CONTRIBUTION TO THE STUDY OF FRACTURE IN AMORPHOUS POLYMERS: EXPERIMENTS AND MODELING

A Thesis

by

ANTHONY DE CASTRO

Submitted to the Office of Graduate Studies of
Texas A&M University
in partial fulfillment of the requirements for the degree of

MASTER OF SCIENCE

December 2010

Major Subject: Aerospace Engineering

CONTRIBUTION TO THE STUDY OF FRACTURE IN AMORPHOUS POLYMERS: EXPERIMENTS AND MODELING

A Thesis

by

ANTHONY DE CASTRO

Submitted to the Office of Graduate Studies of
Texas A&M University
in partial fulfillment of the requirements for the degree of

MASTER OF SCIENCE

Approved by:

Co-Chairs of Committee,	Amine Benzerga
	Ramesh Talreja
Committee Member,	Anastasia Muliana
Head of Department,	Dimitris Lagoudas

December 2010

Major Subject: Aerospace Engineering

ABSTRACT

Contribution to the Study of Fracture in Amorphous Polymers:
Experiments and Modeling. (December 2010)
Anthony De Castro, B.S., Université Technologique de Compiègne, France
Chair of Advisory Committee: Dr. Amine Benzerga

Glassy polymers are extensively used to make all kinds of structural components. Polymers, such as epoxies, are often chosen as matrices in polymer matrix composites (PMC). Ever since the 1960s, these types of composites have been gaining importance in aerospace and automotive advanced applications due to their high stiffness and weight saving potential.

In order to provide clues on the dependence of the fracture behavior upon the stress triaxiality, a series of tensile tests on epoxy (Epon862) round notched bars were carried out at NASA Glenn Research Center. Using state-of-the-art non-contact digital image correlation measurement technique, the mechanical quantities of interest were extracted in order to understand how the fracture behavior responds when subjected to various levels of stress triaxiality induced by varying the notch radius of the specimens. Effects of aging on the fracture behavior were also investigated. A physics-based macromolecular constitutive model that accounts for temperature and pressure sensitivity as well as small-strain softening and large-strain hardening was used to model the deformation behavior. Good correlation between experiments and numerical simulations was achieved. To predict fracture, a pressure-sensitive model motivated by previous work is introduced. Based on the experimental and numerical results, the relation between the mean strain to failure versus the stress triaxiality was defined and it was shown that the fracture response of the material is strongly affected by the level of stress triaxiality.

ACKNOWLEDGMENTS

First and foremost, I would like to express my sincere gratitude to Professor Amine Benzerga for his support and guidance over the last 2 years. His rigor and attention to detail will continue to inspire me.

I would also like to thank Professor Ramesh Talreja and Anastasia Muliana for serving on my thesis committee.

Last, but not least, I would like to thank Soondo Kweon and Xavier Poulain for their support and technical assistance during the course of my research.

TABLE OF CONTENTS

CHAPTER Page

LIST OF TABLES

LIST OF FIGURES

FIGURE Page

FIGURE Page

FIGURE Page

CHAPTER I

INTRODUCTION

Glassy polymers are extensively used to make all kinds of structural components. Polymers, such as epoxies, are often chosen as matrices in polymer matrix composites (PMC). These types of composites have been gaining importance in aerospace and automotive advanced applications due to their high stiffness and weight saving potential. However, their use is limited by their tendency to fail in a macroscopically brittle manner. Little is known about the fracture behavior of epoxies in particular, and polymers in general. In order to better predict when these materials fail, it is necessary to gain knowledge on the driving forces behind their fracture, which ultimately will allow the design and development of more advanced polymers and polymer-based composite materials.

A. Overview of the fracture mechanisms in polymers

Depending on the polymer type, thermoplastic or thermoset, the fracture mechanisms are different. At the molecular scale, for thermoplastics, fracture can occur by breaking of the primary covalent bonds or by the second van der Waals bonds. If an amorphous polymer does not have enough entanglements, its fracture will occur by chain pulling via secondary bond breaking. It usually requires low energy. On

---

The journal model is Comptes Rendus Mécanique.

the other hand, polymers with high entanglement density will fracture via primary bond breaking, which requires higher energy. However, chain scission and chain pull out can occur simultaneously [4]. Fracture mechanisms for thermosets usually occur via primary bond breaking due to their cross-link density, which restrict the polymer network from deforming under an applied load.

In polymers, local inelastic deformations act as a precursor to damage initiation and subsequent propagation, which occur through irreversible changes of microstructure through different complex mechanisms known as crazing and shear yielding. Ductile fracture occurs by the formation of shear band or necking due to intense localized plastic deformation. A high degree of strain softening in a glassy polymer leads to the formation of shear bands. Shear bands are initiated in regions where there are heterogeneities of strain due to surface flaws or internal defects which can produce stress concentrations [5]. Shear bands may be created in tension as well as in compression, and have been observed in a wide range of glassy polymers including PVC, PMMA, epoxy resins, and amorphous PET [5, 6]. On the other hand, the fracture of many polymers is preceded by the formation of crazes. A craze is initiated when an applied tensile stress causes micro-voids to form due to high stress concentration. The micro-voids develop in a plane perpendicular to the maximum tensile stress. The resulting local yield region consists of an interpenetrating network of voids and polymer fibrils as shown in Fig. 1. Unlike a crack, crazes are beneficial to fracture toughness, they are capable of supporting a load and can sometime absorb large amount of strain energy.

Various theories for craze initiation have been proposed. A complex mechanism of craze formation was proposed by Argon et al. [7]. According to them, the event of crazing consists of three distinct steps, which are in order: thermally activated production of stable microporosity under stress; formation of craze nucleus by plastic

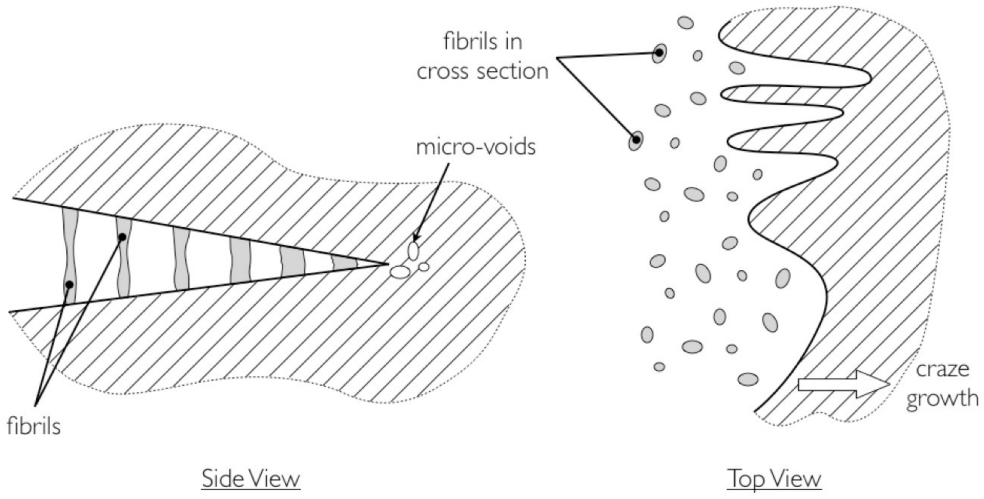

Fig. 1. Craze formation and growth by the meniscus instability mechanism.

expansion of holes in a small region while elastically unloading the surroundings; and extension of the craze nucleus into a planar yield zone. The physical mechanism of craze growth has been successfully explained by the so-called meniscus instability mechanism. The interface between the polymer and the vacuum just outside at the craze tip, does not remain straight but develop into a wavy front and finally break up leaving behind columns of polymer (fibrils) as shown on the top view of Fig. 1. As the front advances, the thickness of the region behind it increases which stretches the fibrils. However, the use of the word stretch here is not appropriate since it has been shown that the fibrils grow mainly by pulling fresh material out of the bulk [8]. Fibrils breakdown ultimately leads to crack growth. It has been shown that fibrils break at the fibril/bulk interface rather than at the so called mid-rib region [9].

B. Influences of the stress state on fracture

Amorphous polymers such as epoxy resins are extensively used as matrix in composite materials. Their combination of high stiffness, strength and low density makes them attractive for all kind of advanced structural applications. However, the polymer matrix must sustain local multi-axial stresses originating not only from the loading conditions but also from the reinforcement itself [10]. Surprisingly little is known about how these materials fracture when subjected to these stress states.

By way of contrast, for metals, this subject has been studied to a great extent with a rich experimental database and good physical understanding of the factors governing the onset of fracture. One way to experimentally reproduce a multi-axial stress state is to perform test on round notched bar specimens. This has been done extensively to investigate the effect of stress triaxiality on fracture strain for metals [11, 12, 13, 14]. By varying the notch radius, one is able to introduce different intensity levels of stress triaxiality. Bridgman was the first to analyze the stress distribution in round bar specimens with different notches and to give experimental evidence of the effect of the stress state on the strains to failure in tension for steels [15].

However, to date, similar investigations are very scarce for polymers in general, and almost inexistent for amorphous polymers in particular. Tensile experiments were carried on polycarbonate (PC) notched round bars by Wang et al. [2] at room temperature. The notch radii (R) were 0.8, 1.2, 2, 4 and 8 mm. Smooth specimens were also tested ($R \rightarrow \infty$). The fracture strain ϵ_c was calculated from the variations in the minimum diameter of the notch:

$$\epsilon_c = 2 \ln \left(\frac{D_0}{D_c} \right) \tag{1.1}$$

where D_c is the critical value of the diameter at the minimum cross-section, and D_0

the corresponding initial value. In order to characterize the level of stress triaxiality induced by the different notch radii, they used the Bridgman formula commonly used with metals notched bar [15]:

$$\frac{\sigma_m}{\sigma_{eq}} = \frac{1}{3} + \ln\left(1 + \frac{D}{4R}\right) \tag{1.2}$$

where σ_m is the mean (hydrostatic) stress, σ_{eq} is the von Mises equivalent stress, R is the notch radius and D is the specimen's minimum cross-section current diameter. They showed, Fig. 2, that the strain to fracture for their material was decreasing as the stress triaxiality ratio was increasing. In other words, the higher the stress triaxiality, the more brittle the fracture mode of PC becomes.

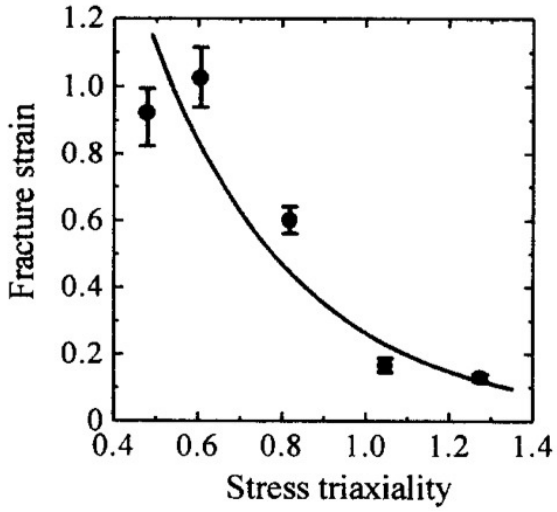

Fig. 2. Effect of the stress triaxiality on the strain to fracture of PC [2].

Similarly, Sobieraj et al. [16] studied the effect of pressure on fracture of notched cylindrical bars of conventional and ultra-high molecular weight polyethylene (UHMWPE). They showed that the triaxial stress state induced by the notch has a strong impact on the fracture behavior. Moreover, Kody et al. [17, 18] also investigated the effect

of hydrostatic pressure on polymer fracture. Using epoxies with different molecular weight ranging from 380 to 1790 g/mol, they casted the resins into thin-walled hollow cylinders where pressure was applied internally. They carried out tension and compression tests on the hollow specimens and concluded that the fracture response of their epoxies was strongly affected by the stress state.

While experimentally it has been proven that fracture behavior of amorphous polymers, such as epoxies, is strongly affected by local stress states, to date, the relationship between strain to fracture and stress triaxiality is still unclear and further work is needed to construct a fracture locus which, ideally, would cover a wide range of stress triaxiality.

C. Effect of physical aging on the fracture behavior

Struik [19] defined isothermal structural relaxation below the glass transition temperature (T_g) of materials as physical aging. Structural relaxation is a phenomenon that occurs in amorphous glassy polymers below their T_g. Upon quenching from a temperature above T_g, the material is not given sufficient time to reach its equilibrium state. Its specific volume is initially in a non-equilibrium state and slowly approaches equilibrium value with time. This process of slow evolution towards an equilibrium state is known as physical aging. It is to be distinguished from chemical aging, which involves some degree of chemical degradation of the material, such as thermal degradation or photo-oxidation. In general, glassy polymers become stiffer and more brittle when aged, mechanical properties such as creep rate, the strength [20] and to a lesser extent, the impact fracture energy [21], are altered by this process. There is indication from the literature that many aspects of physical aging are

common to both thermoplastic and thermosetting materials [19, 20, 22].

Very limited work has been done to date to study the effect of aging on fracture behavior of glassy amorphous polymers. Kong [3] investigated the aging phenomenon on fracture properties of postcured epoxy resin and epoxy resin reinforced with carbon fibers. In order to avoid chemical aging due to ultra violet light irradiation, the experiment was designed in a dry, dark and inert atmosphere. With the exception of a few samples, the dog-bone-shaped specimens were postcured to render a fully-crosslinked network, then heated to 260°C for 20 minutes and finally immediately air-quenched to room temperature. Some of those specimens were tested right away, the rest were annealed at either 80, 110 or 140°C for time increments of 10, 10^2, 10^3, 10^4 and up to 10^5 minutes. The effect of physical aging at 140°C on the ultimate tensile strength are shown in Fig. 3 (a). The effect of thermal history on the ductility of epoxy are summarized in Fig. 3 (b).

The results showed that as physical aging proceeds, the fracture behavior of the epoxy polymer is clearly affected with a decrease in its ultimate mechanical properties such as its ultimate tensile strength and its strain to failure. The polymer fractures in a more brittle fashion with aging.

D. Modeling fracture in amorphous polymers

Numerous theories and models have been developed during the last 40 years for modeling polymers fracture behavior. Most studies on fracture of amorphous glassy polymers are based on linear elastic fracture mechanics [23, 24]. However, Estevez et al. [25] pointed out that this approach hides the process of initiation, widening and breakdown of crazes which is responsible for crack creation. Classical fracture

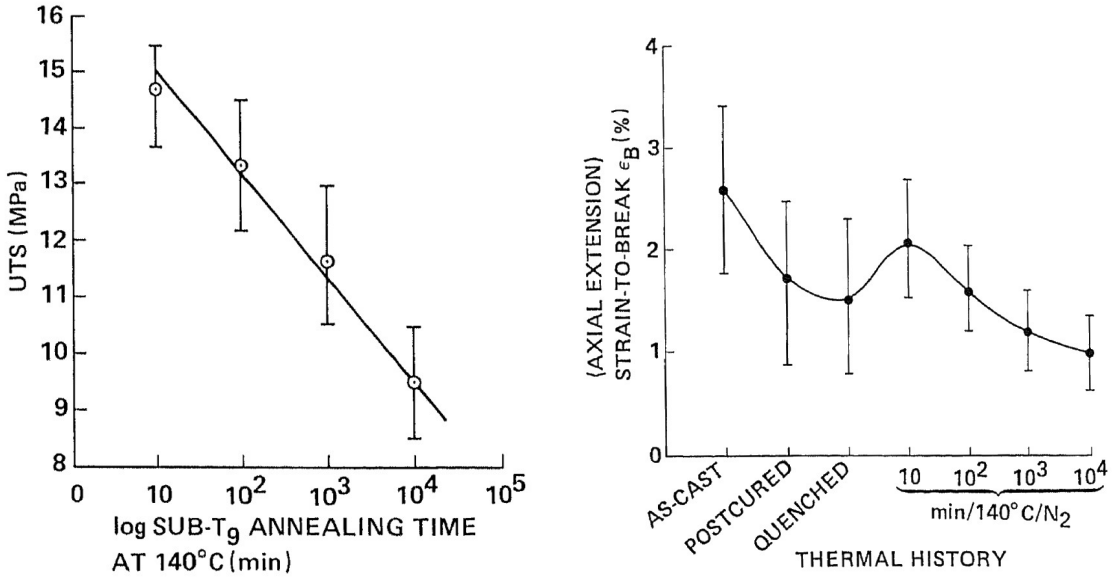

(a) (b)

Fig. 3. Effect of aging on neat epoxy resin [3],
(a) Ultimate tensile strength of postcured epoxy as a function of aging time
(b) Ductility as a function of thermal history.

mechanics cannot deal with crack nucleation, and the numerical simulation of crack propagation has also been a challenge for this classical theory.

One of the earliest model that deals with craze nucleation is a stress based craze initiation criterion developed by Sternstein et al. [26, 27] based on experiments on poly(methyl methacrylate) (PMMA) plates with a circular hole under biaxial tension. The underlying assumption behind their criterion is that the polymer free volume, in large amount in amorphous polymers, is increased due to the dominance of dilative stresses, which ultimately facilitates molecular orientation and mobility of chain segments leading to the formation of voids and fibrils. Oxborough et al. [28], based on their own experiments on polystyrene (PS), developed an alternative criterion which postulates that crazes initiate when the maximum principal tensile

strain reaches a critical value which depends on the mean normal stress. Gearing et al. [29] further rearranged Browden's initiation criterion from a critical strain-based criterion to a critical stress-based criterion, in which craze initiates when the maximum principal stress reaches a critical value which depends on the mean normal stress and two temperature dependent material parameters.

Once crazes have initiated, growth occurs due to extension of the fibrils in the direction of the maximum principal stress, which leads to an advancing craze tip perpendicularly to this direction. In order to model craze growth and breakdown, Gearing et al. [29] adopted a model where the viscoplastic flow rule, for the general polymer deformation, switches to a craze flow rule once initiation has started. Chowdhury et al. [30] pointed out that Gearing's model does not account for gradual loss of stress bearing capacity of the crazes structure and that craze breakdown is considered by imposing an ad-hoc critical strain criterion which is empirically defined. Based on Gearing's work, Chowdhury et al. [31] proposed an improved model that accounts for craze initiation, craze growth process associated with fibril formation and breakdown, accompanied by gradual loss of load bearing capacity and final failure of the crazes structure.

CHAPTER II

TENSILE TESTS ON NOTCHED ROUND BARS

A. Introduction

An experimental plan has been defined which mainly aims at investigating the effect of stress triaxiality on macroscopic measures of fracture. The experimental data basis was generated using custom designed test specimens. These were round notched bars where the notch acuity implies a specific amount of stress triaxiality. This type of specimens is commonly used to investigate fracture in ductile and brittle metals [32]. The locus of strain-to-failure versus a measure of stress triaxiality[1] will be referred to as the fracture locus of the material. The underlying hypothesis of this work is that the amount of hydrostatic stress superposed onto a given deviatoric loading affects the strain to failure. There has been some indication in the literature that pressure effects are important in thermoplastic polymers. To date, no detailed experimental work has been conducted yet to determine the fracture locus for thermosetting polymers in general and epoxies in particular. In addition, in this work the influence of test temperature, strain rate and physical aging were also investigated.

[1] These quantities will be precisely defined later.

B. Presentation of the experiments

A series of epoxy (EPON 862) notched round bars have been tested in tension under various strain rates ranging from 10^{-5} to 10^{-1}/s and temperatures ranging from room temperature to 80°C. The tests were conducted at NASA Glenn Research Center by two undergraduate student from Texas A&M University, B. Burgess and T. Woodbury. The mechanical quantities of interest were measured using optical measurement techniques. These tests demonstrated the effects of stress state, strain rate and temperature not only on the deformation behavior but also on the fracture response of the epoxy.

1. Material and specimens

The material used in this study is an epoxy resin (Epon 862) cured at 176°C for 2.5 hours under 1.03 MPa of pressure. Table I summarized the material properties. Experiments from Littell et al. [33] for smooth round bars of the same material have been performed to determine the polymer's intrinsic behavior.

Table I. Material properties.

Density	Poisson's ratio	Young's modulus [1]	T_g [2]
1100 kg/m^3	0.4	2.6 GPa	109°C

[1] *at room temperature* [2] *Glass transition temperature*

The specimens were designed based on previous studies for ductile fracture in metals [14]. The bars were machined from stock sheets of epoxy resin plates of 60.96 mm×60.96 mm×6.35 mm. The result was tightly controlled specimen geometry

with a very smooth surface finish. The precise machining method used allowed for minimal variations between the specimens. Fig. 4 shows an example of the specimen tested.

Fig. 4. Example of a generic test specimen.

In order to vary the stress triaxiality, three notch radii were considered: R=0.78 mm, R=1.56 mm and R=3.9 mm. The dimensions of the specimens are shown in Fig. 5. To each notched specimen corresponds an expected level of stress triaxiality. Each geometry is identified by the parameter ζ with $\zeta/10$ being equal to the ratio of notch radius to the minimal section diameter. Decreasing value of ζ translates into a more intense triaxial stress state.

2. Setup and measurements

The specimens were tested in tension at various temperatures (25°C, 50°C and 80°C) at different levels of nominal strain-rate (10^{-5}/s, 10^{-3}/s and 10^{-1}/s). Up to four (4) realizations of each test condition (type of notch, temperature and strain rate) were obtained. The specimens were placed between grips of an axial-torsional MTS servo-hydraulic machine (Fig. 6a). At higher temperatures, a boro-silicate glass temperature chamber was used (Fig. 6b). Isothermal conditions were reached by heaters and thermocouples suitably located around the specimen ensured a uniform temperature (within 1°C) between the specimen surface temperature and the surrounding air. Full-field surface strain measurements were carried out using a precise non-contact digital image correlation technique. Each tested specimen was painted with a black and white speckled pattern (Fig. 7) such that displacements and rotations of the

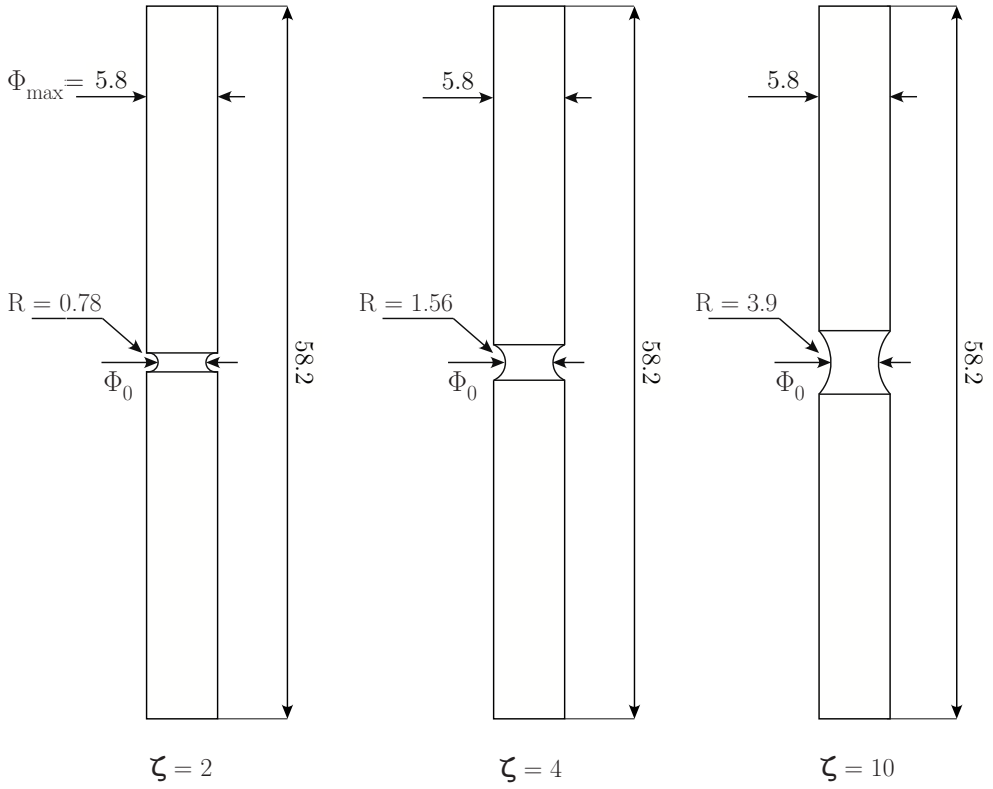

Fig. 5. Geometry of round notched bars with $\Phi_0 = 3.9$ mm, R the notch radius and $\zeta = 10 \times R/\Phi_0$.

speckles were tracked during the test by two cameras. Figure 8 shows a close-up of a mounted specimen, for both the room temperature setup and the high-temperature setup.

Image data processing was carried out using the Aramis software, which provided the pointwise dilatational and shear strains. A detailed mapping of local surface strains could therefore be obtained, as illustrated in Fig. 9. However, the resolution of strain measurement is not sufficient to detect strain concentrations in areas where fracture eventually initiates. In addition, the initiation point is often located in the interior of the specimen, as will be shown below thanks to fractographic examination.

(a)

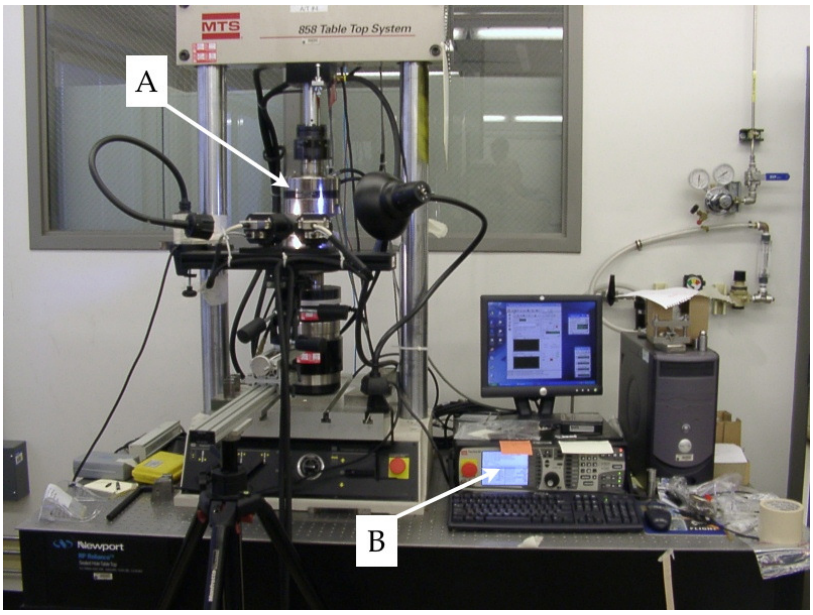

(b)

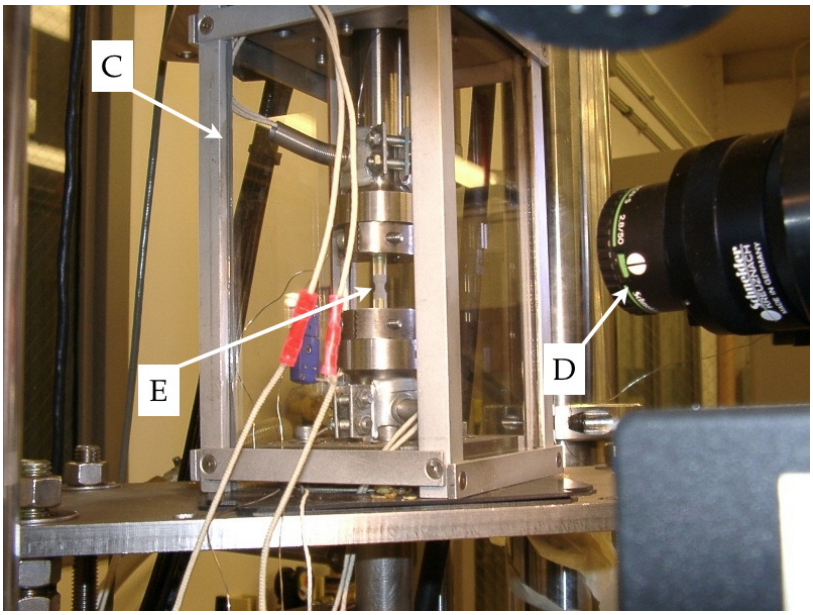

Fig. 6. (a) Setup for room temperature testing (A: MTS machine, B: MTS computer controller, temperature chamber control box and ARAMIS data acquisition computer.) (b) Setup for high temperature testing (C: Temperature chamber, D: Optical measurement cameras, E: Specimen tested).

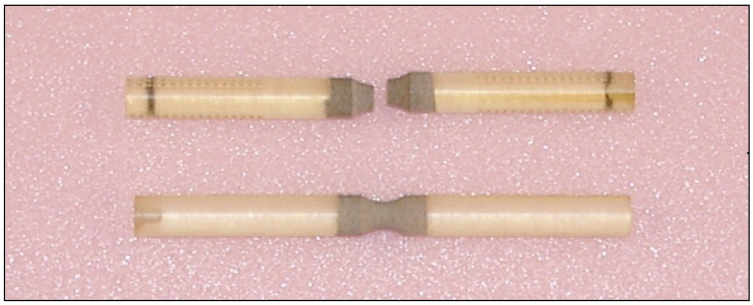

Fig. 7. Notched specimen with speckles before testing (bottom) and post-test (top).

Therefore, in order to quantify the strain to failure, the following specimen-level measure was defined:

$$\bar{\varepsilon} = \ln \frac{S_0}{S} = 2 \ln \frac{\Phi_0}{\Phi} \tag{2.1}$$

where S is the current notch-root cross-sectional area, Φ is the corresponding diameter and the subscript 0 refers to initial values. The above strain measure represents the average total strain in the section of minimal diameter. In particular, its values at crack initiation, $\bar{\varepsilon}_\mathrm{i}$, and after complete failure of the bar, $\bar{\varepsilon}_\mathrm{f}$ can be defined using the corresponding values of Φ_i and Φ_f, respectively. In actuality, the crack propagation stage is so sudden that the distinction between $\bar{\varepsilon}_\mathrm{i}$ and $\bar{\varepsilon}_\mathrm{f}$ is impossible. Had they been measured separately, it is likely that these two strains would be very close from each other. Thus, we will only invoke strains to failure initiation $\bar{\varepsilon}_\mathrm{i}$ in the sequel. For simplicity, the above strain measure is termed *mean strain to failure*.

Definition (2.1) requires that the diameter Φ be measured at the desired location. This was carried out using the post-processing capabilities of the Aramis software. More specifically, the tangent circle method was used as sketched in Fig. 10.

(a)

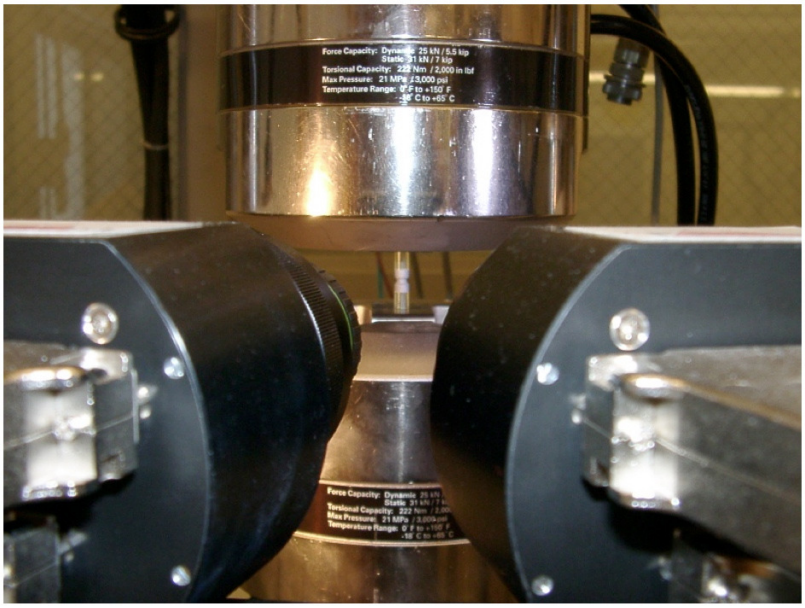

(b)

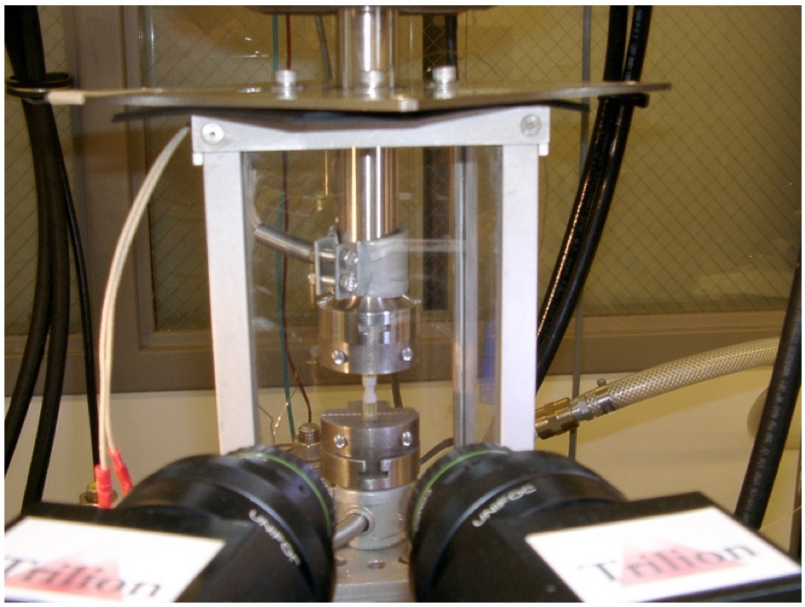

Fig. 8. (a) Painted notched bar mounted for room-temperature testing. (b) Painted notched bar mounted for high-temperature testing.

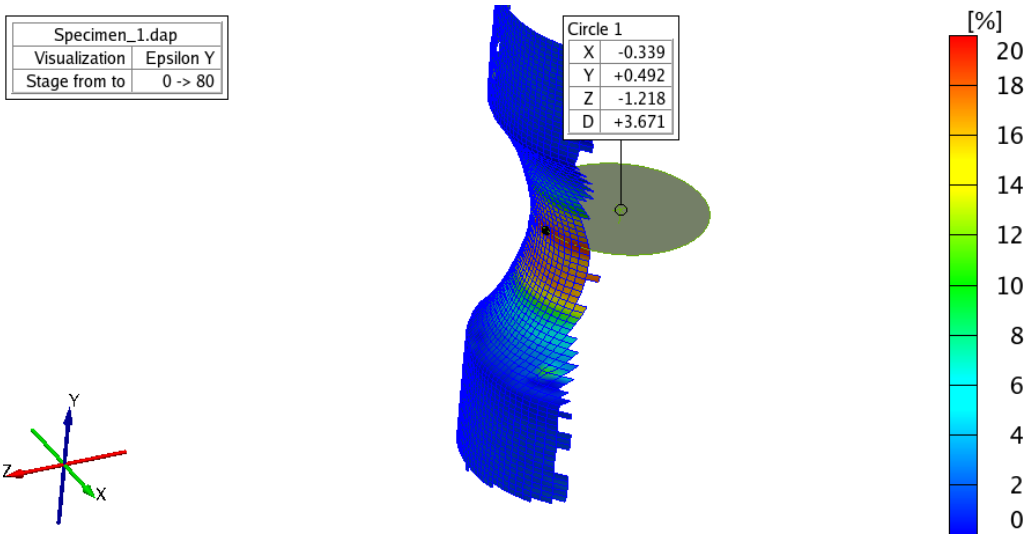

Fig. 9. Contours of extensional axial strain in a typical notched bar experiment using the digital image analysis software Aramis. Also shown is the tangent circle used to determine the current cross-sectional diameter Φ in (2.1).

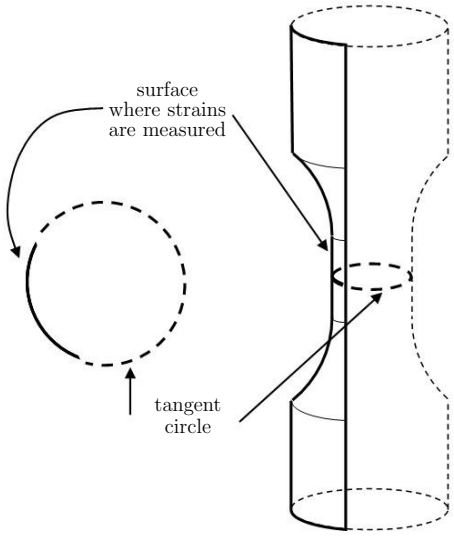

Fig. 10. Determination of the current cross-sectional diameter Φ using the tangent circle method (Aramis post-processing).

C. Discussion of the results

1. Tensile tests results

The fracture locus of the material is defined as a measure of fracture property (mean strain to failure) versus a measure of stress state (stress triaxiality ratio). To quantify the triaxiality of the stress state, a stress triaxiality ratio, τ, is defined as:

$$\tau = \frac{\sigma_m}{\sigma_{eq}} \tag{2.2}$$

where σ_m denotes the mean normal stress (i.e. hydrostatic stress $= \sigma_{kk}/3$) and σ_{eq} is the von Mises equivalent stress. Expectations based on the original design of the specimens and elastoplastic finite-element simulations of the tests using power-law hardening materials lead to the following values of the triaxiality, averaged over the history and the notch-root cross-section: 0.6–0.8 ($\zeta = 10$); 0.9–1.1 ($\zeta = 4$) and 1.2–1.4 ($\zeta = 2$).

With the measure of the minimal cross section S_0, curves of normalized load F/S_0 versus mean strain $\bar{\epsilon}$ were plotted for the various notch acuities, temperatures and strain rates. Each experiment was repeated such that between two and four load–deformation curves could be drawn for each condition. Figure 11 depicts the effect of notch acuity on the load–deformation response. The sample results are shown for $T = 25$C (Fig. 11a) and $T = 80$C (Fig. 11b)[2]. Irrespective of the temperature, the load is higher in a bar with a sharp notch ($\zeta = 2$) than in one with a shallow notch ($\zeta = 10$), as expected. The load carried by the moderately notched bar ($\zeta = 4$) is in between, on average. However, the variation of the peak load with the notch acuity is weaker than expected. The fact that the level of axial load does not vary much from

[2]The zigzagged character of the curves at small deformation levels is due to inaccuracies in the measurement of the diameter.

(a)

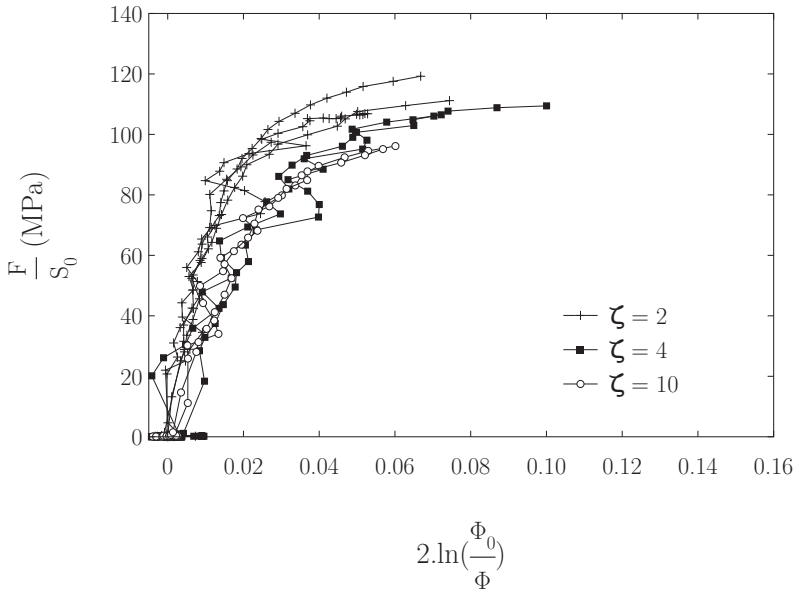

(b)

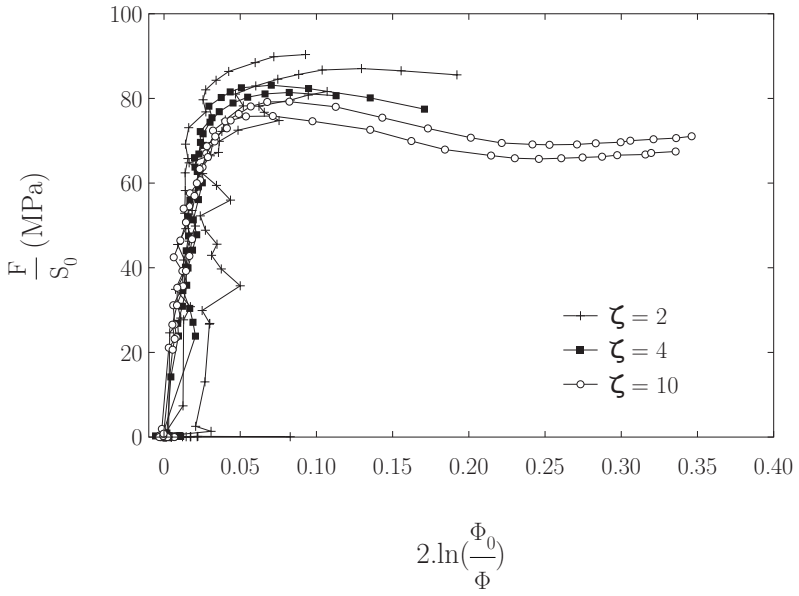

Fig. 11. Normalized load versus minimal cross-section mean strain at $\dot{\epsilon} = 10^{-1}$/s for various levels of triaxiality. (a) $T = 25°$C. (b) $T = 80°$C.

one geometry to the other indicates that the stress triaxiality does not vary by the amount expected based on the FE analyses that were used to design the experiments. *Part of this unexpected trend may be associated with the changes made to specimen dimensions. An other part may be due to the peculiar behavior of Epon 862, which does not follow a power-law hardening. For more details see chapters IV–C and IV–D.* Also, similar results for a different strain rate can be found in Appendix A. It is important to keep this limitation in mind as the results are presented from both experiments and analysis.

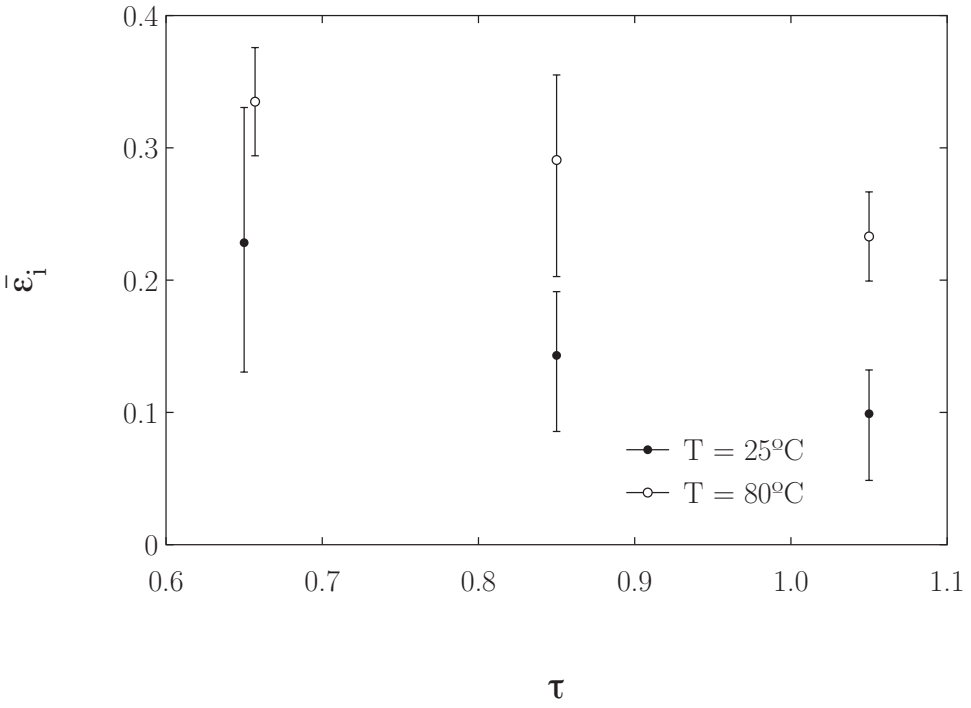

Fig. 12. Minimal cross-section mean strain to fracture versus triaxiality ratio at $\dot{\epsilon} = 10^{-3}$ s^{-1} for $T = 25°$C and $T = 80°$C.

Although the stress triaxiality τ in (2.2) may not vary between the bars by as much as expected, the results in Fig. 11 indicate a consistent trend for a decreasing ductility with increasing τ, the strains to failure being smaller in bars with a sharp

notch. This trend is summarized in Fig. 12 which depicts examples of the so-called fracture loci[3]. Note that the strain rate is lower here than in Fig. 11. Also note the scatter in the values of the mean strain to failure around the average value (indicated by a point). This scatter is associated with the fact that fracture is not deterministic. For example, one origin of the scatter is the slight variation in the initiation location.

In addition to the main effect of stress triaxiality, the effect of temperature on ductility and on the "fracture locus" is clearly seen in Figs. 11 and 12 (compare parts (a) and (b) in Fig. 11). Some of the corresponding load–deformation curves are shown in Fig. 13. As expected from smooth bars testing, there is some thermal softening: the strength decreases with increasing temperature. At all triaxiality levels, this thermal softening leads to a greater ductility. At low triaxiality levels ($\zeta = 10$), the scatter is very large so that the above trend may not be very clear from Fig. 13b;

2. Fracture surfaces

In addition to the stress–strain curves generated from the experimental results, pictures of the fracture surfaces of each notched specimen were taken postmortem using a low powered optical microscope in order to determine the nature and the initiation point of each fracture event. Figure 14 and 15 summarized the two main fracture initiation sites. It was observed that the stress triaxiality intensity induced by the different notch radii have a strong correlation with the location where fracture initiates. In the case of a sharp notch acuity, Fig. 14, the onset of fracture is mostly located in the vicinity of the specimen's notch root whereas in the case of a less sharp notch acuity, for Fig. 15, it is located near the specimen's center.

[3]The values assigned to τ in the abscissa are based on the FE analyses mentioned

(a)

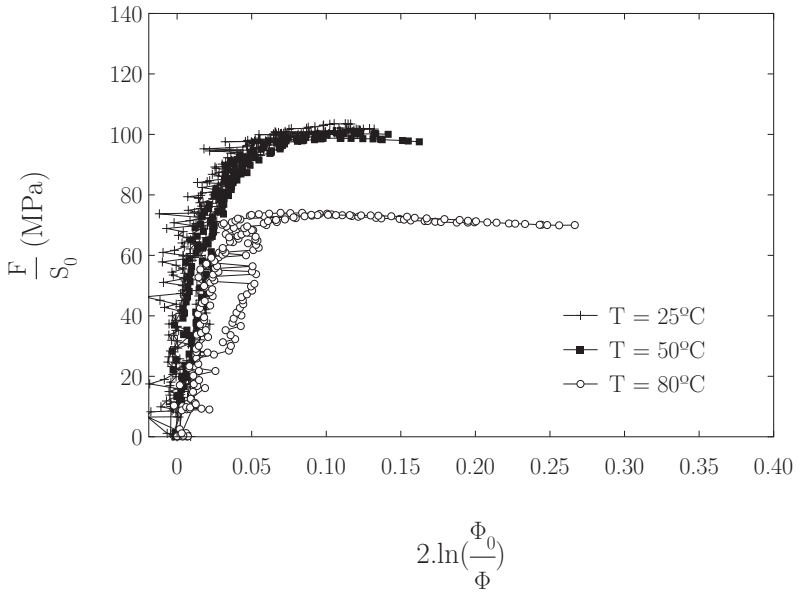

(b)

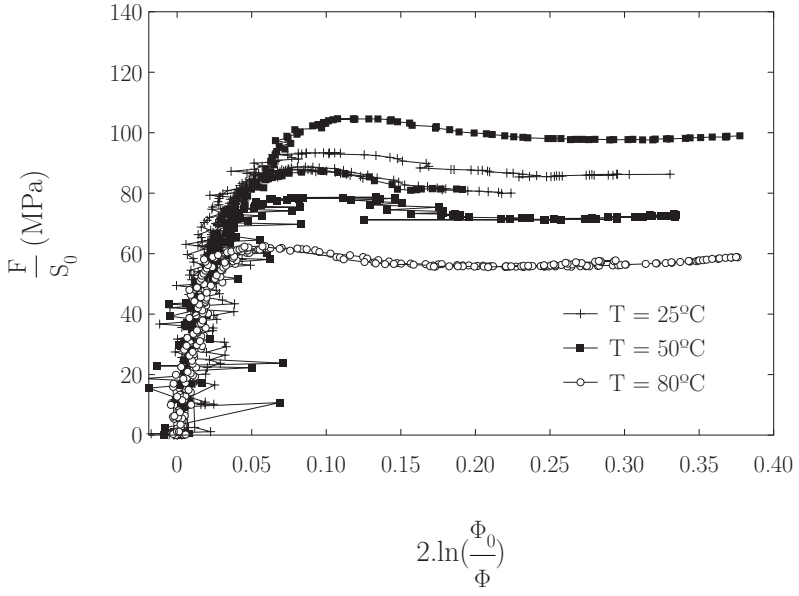

Fig. 13. Normalized load versus minimal cross-section mean strain at $\dot{\epsilon} = 10^{-3}$ s^{-1} and various levels of temperature. (a) $\zeta = 2$. (b) $\zeta = 10$.

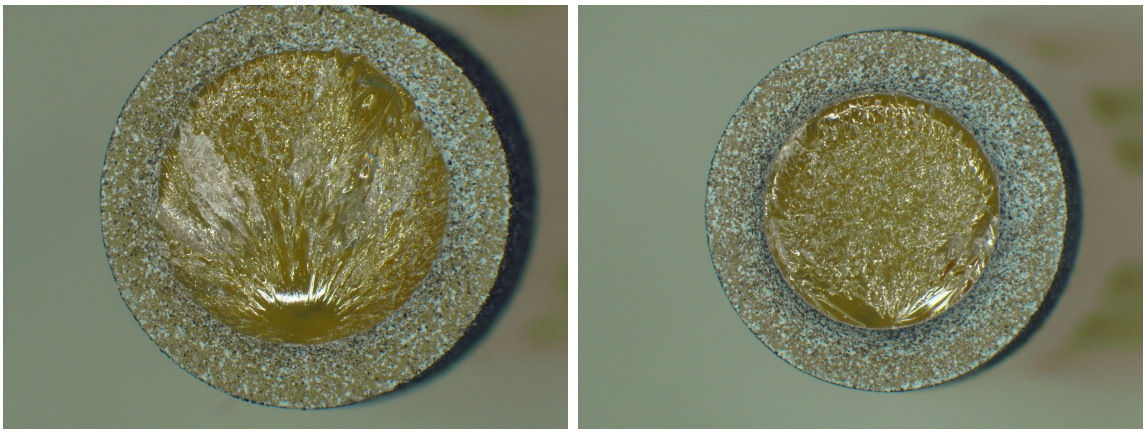

(a) Realization #1 (b) Realization #2

Fig. 14. Fracture surface of a sharp notched specimen ($\zeta = 2$) tested at $\dot{\epsilon} = 10^{-3}$/s and $T = 25°$C.

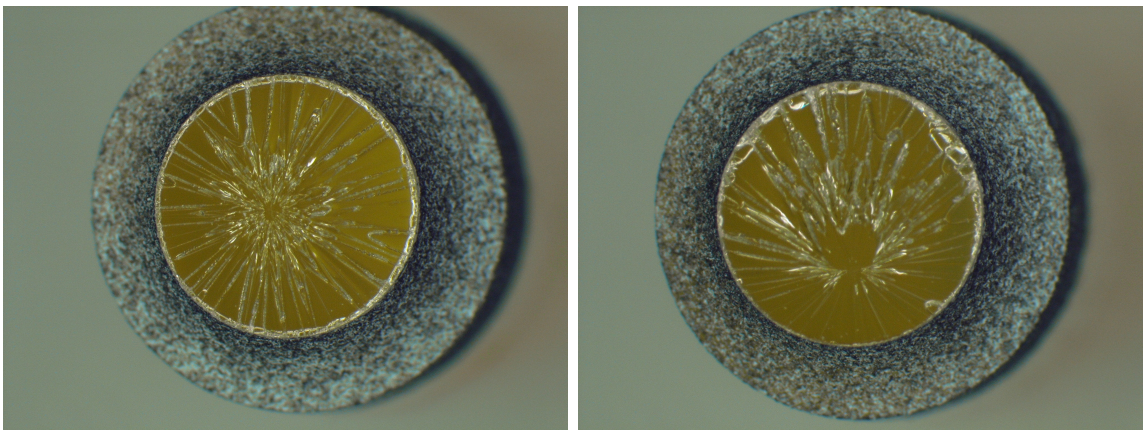

(a) Realization #1 (b) Realization #2

Fig. 15. Fracture surface of a medium notched specimen ($\zeta = 4$) tested at $\dot{\epsilon} = 10^{-1}$/s and $T = 50°$C.

A complete summary of the locations of fracture initiation for all specimens tested is shown in Fig. 16. When fracture initiates near the specimen's center, the location is defined as "Internal" and when it initiates near the notch root, the location is defined as "External".

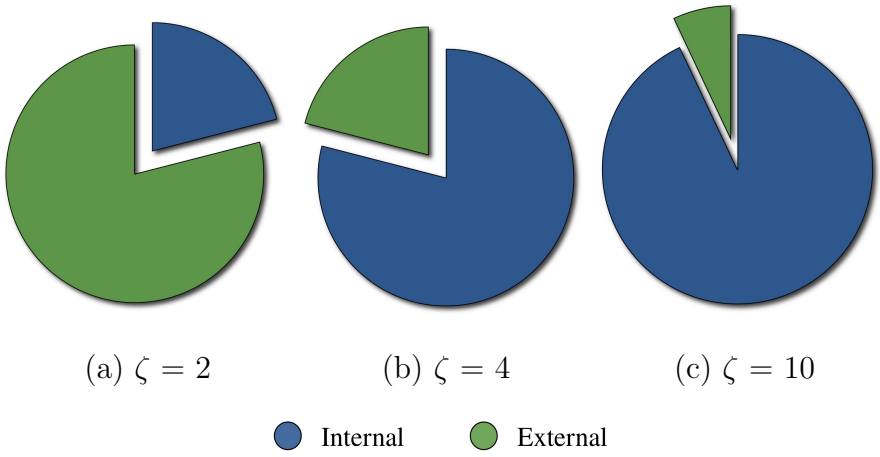

Fig. 16. Summary of the locations of fracture onset for all temperatures, strain rates and notch radii.

As the stress triaxiality increases in intensity, the location of the onset of fracture switches from a region near the specimen's center to the notch root vicinity.

D. Conclusions

A series of tensile tests on epoxy round notched bars were carried out in order to provide clues on the dependence of the fracture behavior upon the stress triaxiality. Results have shown a strong effect of the level of stress triaxiality, induced by the specimen notch radius, on the strain to failure. However, it has been shown that the variation of stress triaxiality levels is weaker than expected based on the FE

above. Thus, they are only indicative.

simulations that were used to design the experiments. In order to further investigate these unexpected trends, it is necessary to capture the variations of the stress state induced by the different specimen geometries and to gain knowledge of the local mechanical quantities of interest. To achieve this goal, numerical simulations were used.

CHAPTER III

MODELING OF THE MATERIAL DEFORMATION

A. Introduction

The so-called macromolecular model is the result of approximately 40 years of collaborative work on modeling complex glassy polymer behavior. First, Haward et al. [34] developed a one dimensional continuum model, by using the Eyring dashpot model to describe yield and Langevin spring model to describe post yield orientational hardening behavior. Then, Argon [35] incorporated dependence upon strain rate. Later, Boyce et al. [36] improved the model by incorporating hydrostatic pressure sensitivity, three dimensional effect, finite strain kinematics and classical three chain rubber elasticity model to describe the orientation hardening. Arruda et al. [37] further refined the model by considering thermal softening due to adiabatic heating. Wu et al. [38] revised Boyce model by improving the orientation hardening in considering a statistical combination of three chain and eight chain rubber elasticity model. Finally, the model as been modified by Chowdhury et al. [31] to better represent the small strain behavior with the possibility to model independently the pre-peak hardening and the post-peak softening observed in amorphous polymers. As it is showed in the next chapter, the basis of the macromolecular model is to combine a rate-sensitive plastic flow rule with an anisotropic hardening model.

B. Formulation

First, an additive decomposition of the total rate of deformation $\mathbf{D}$ into an elastic and a plastic part is assumed. A hypoelastic law is used to specify the elastic part $\mathbf{D}^{\mathrm{e}}$ in terms of the co-rotational rate of Cauchy stress as:

$$\mathbf{D}^{\mathrm{e}} = \mathbf{L}^{-1} : \overset{\nabla}{\boldsymbol{\sigma}} \tag{3.1}$$

where $\mathbf{L}$ is the point-wise tensor of elastic moduli given in terms of Young's modulus and Poisson's ratio as follows:

$$L_{ijkl} = \frac{E}{1+\nu}\left[\frac{1}{2}(\delta_{ik}\delta_{jl} + \delta_{il}\delta_{jk}) + \frac{\nu}{1-2\nu}\delta_{ij}\delta_{kl}\right] \tag{3.2}$$

and $\overset{\nabla}{\boldsymbol{\sigma}}$ is the co-rotational rate of Cauchy stress.

In the polymer matrix, the flow rule is specified such that plastic deformation is incompressible, i.e.,

$$\mathbf{D}^{\mathrm{p}} = \dot{\epsilon}\,\mathbf{p}, \quad \mathbf{p} = \frac{3}{2\sigma_{\mathrm{e}}}\boldsymbol{\sigma}'_{\mathrm{d}} \tag{3.3}$$

where $\dot{\epsilon}$ is the effective strain rate, describing the magnitude of the plastic flow, defined as:

$$\dot{\epsilon} = \sqrt{\frac{2}{3}\,\mathbf{D}^{\mathrm{p}'} : \mathbf{D}^{\mathrm{p}'}} \tag{3.4}$$

and p being a tensor that defines the direction of the plastic flow. Also, $\mathbf{X}'$ refers to the deviator of second-rank tensor $\mathbf{X}$, and σ_e is an effective stress defined by:

$$\sigma_{\mathrm{e}} = \sqrt{\frac{3}{2}\boldsymbol{\sigma}'_{\mathrm{d}} : \boldsymbol{\sigma}'_{\mathrm{d}}} \tag{3.5}$$

with $\boldsymbol{\sigma}_{\mathrm{d}} = \boldsymbol{\sigma} - \mathbf{b}$ being the driving stress and $\mathbf{b}$ the back stress tensor that describes

the orientation hardening of the material. It evolves following:

$$\overset{\nabla}{\mathbf{b}} = \mathbf{R} : \mathbf{D} \tag{3.6}$$

$\mathbf{R}$ being a fourth-order tensor, which is specified here by using a non-Gaussian network model [39] that combines the classical three-chain rubber elasticity model [36] and the eight-chain model [40], such that

$$\mathbf{R} = (1-\kappa)\,\mathbf{R}_{\text{3-ch}} + \kappa \mathbf{R}_{\text{8-ch}} \tag{3.7}$$

where $\kappa = 0.85\bar{\lambda}/\sqrt{N}$, N is a material constant and $\bar{\lambda}$ is the maximum principal stretch, which is calculated based on the left Cauchy–Green tensor $\mathbf{B} = \mathbf{F} \cdot \mathbf{F}^T$, and the contravariant components of the eight-chain back-stress moduli tensor, $\mathbf{R}_{\text{8-ch}}$, are given by

$$R^{\text{8-ch}}_{ijkl} = \frac{1}{3} C^R \sqrt{N} \left[\left(\frac{\xi_c}{\sqrt{N}} - \frac{\beta_c}{\lambda_c} \right) \frac{B_{ij} B_{kl}}{B_{mm}} + \frac{\beta_c}{\lambda_c} \left(\delta_{ik} B_{jl} + B_{ik} \delta_{jl} \right) \right] \tag{3.8}$$

where B_{ij} are the components of the left Cauchy-Green tensor. C^R and N are material constants known as the rubbery modulus and average number of links between entanglements, respectively, and

$$\lambda_c^2 = \frac{1}{3} tr\mathbf{B}, \quad \beta_c = \mathcal{L}^{-1}\left(\frac{\lambda_c}{\sqrt{N}} \right), \quad \xi_c = \frac{\beta_c^2}{1 - \beta_c^2 csch^2 \beta_c} \tag{3.9}$$

where $\mathcal{L}^{-1}$ is the inverse Langevin function defined as $\mathcal{L}(x) = \coth x - \frac{1}{x}$. The components of $\mathbf{R}_{\text{3-ch}}$ are given in terms of the principal total stretches λ_I, with respect to axes pointing onto the principal stretch directions,

$$R^{\text{3-ch}}_{IJKL} = \frac{1}{6} C^R \sqrt{N} {\lambda_I}^2 \left(\frac{\xi_I}{\sqrt{N}} + \frac{\beta_I}{\lambda_I} \right) \left(\delta_{IK}\delta_{JL} + \delta_{JK}\delta_{IL} \right) \quad if\ I = J \tag{3.10}$$

$$R^{\text{3-ch}}_{IJKL} = \frac{1}{6}C^R\sqrt{N}\frac{{\lambda_I}^2 + {\lambda_J}^2}{{\lambda_I}^2 - {\lambda_J}^2}(\lambda_I\beta_I - \lambda_J\beta_J)(\delta_{IK}\delta_{JL} + \delta_{JK}\delta_{IL}) \quad if\ I \neq J \tag{3.11}$$

Strain rate effects are accounted for through a viscoplastic law giving the effective plastic strain rate $\dot{\bar{\epsilon}}$ in (3.3) as [35, 36]:

$$\dot{\bar{\epsilon}} = \dot{\epsilon_0}\exp\left[-\frac{A\left(s - \alpha\sigma_h\right)}{T}\left(1 - \left(\frac{\sigma_e}{s - \alpha\sigma_h}\right)^m\right)\right] \tag{3.12}$$

where $\dot{\epsilon}_0$, m and A are material parameters, α is a factor describing pressure sensitivity, T is the absolute temperature, $\sigma_h = tr\boldsymbol{\sigma}$ is the trace of Cauchy stress and s is a micro-scale athermal shear strength. Boyce et al. [36] introduced strain softening effects through the state variable s. In order to better represent the small strain behavior, [31] modified the evolution law for s (from its initial value s_0 to its current value s) as follows:

$$\dot{s} = h_1(\bar{\epsilon})\left(1 - \frac{s}{s_1}\right)\dot{\bar{\epsilon}} + h_2(\bar{\epsilon})\left(1 - \frac{s}{s_2}\right)\dot{\bar{\epsilon}} \tag{3.13}$$

where s_1 and s_2 are adjustable parameters and $h_1(\bar{\epsilon})$ and $h_2(\bar{\epsilon})$ are smooth, Heaviside-like functions given by:

$$h_1(\bar{\epsilon}) = -h_0\left\{\tanh\left(\frac{\bar{\epsilon} - \bar{\epsilon}_p}{f\bar{\epsilon}_p}\right) - 1\right\}; \quad h_2(\bar{\epsilon}) = h_0\left\{\tanh\left(\frac{\bar{\epsilon} - \bar{\epsilon}_p}{f\bar{\epsilon}_p}\right) + 1\right\} \tag{3.14}$$

The updating of the back stress $\mathbf{b}$ is obtained using $\mathbf{b}_{t+\triangle t} = \mathbf{b}_t + \triangle t\dot{\mathbf{b}}$ with the convected rates calculated through

$$\dot{\mathbf{b}} = \overset{\triangledown}{\mathbf{b}} - \mathbf{bD} - \mathbf{Db} \tag{3.15}$$

This constitutive model has been implemented in a user-defined routine (UMAT)

in the commercial finite element code ABAQUS. Here, large strains are modeled within objective space frames. Implementation of the macromolecular model as a UMAT thus requires to recast the constitutive equations using a co-rotational formulation [41].

C. Results

Finite element models were built in Abaqus/Standard to simulate the experiments. For round bars, axisymmetric elements were used. Due to symmetry, only a quarter of the specimen was modeled, see Fig. 17.

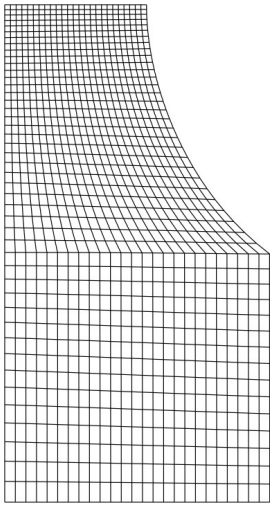

Fig. 17. Example of a finite element model of a round notched specimen.

Details on the procedure to identify the material parameters can be found in Poulain's work [1]. The following numerical results were all obtained from the macromolecular model simulations calibrated with the material parameters identified by Poulain. Table II summarized the materials parameters used to calibrate the model.

The predictive capabilities of the model implemented in Abaqus via a user-defined routine (UMAT) are tested against the experimental results at various levels of pressure, temperature and strain rate. Overall, the numerical simulations are in good agreement with the experimental results. The deformation behavior of Epon 862 is very well captured for all notch acuities as illustrated in Figure 18 which corresponds to specimens tested at a temperature $T = 25°\text{C}$ and a strain rate $\dot{\epsilon} = 10^{-1}/\text{s}$ for all three notch radii.

Similarly, the model shows very good agreement with the temperature, Fig. 19, and strain rate dependence, Fig. 20, of the material deformation. Also, it can be observed in Fig. 19, which corresponds to a shallow notched specimen, that the model is able to capture the softening stage occurring at large strains.

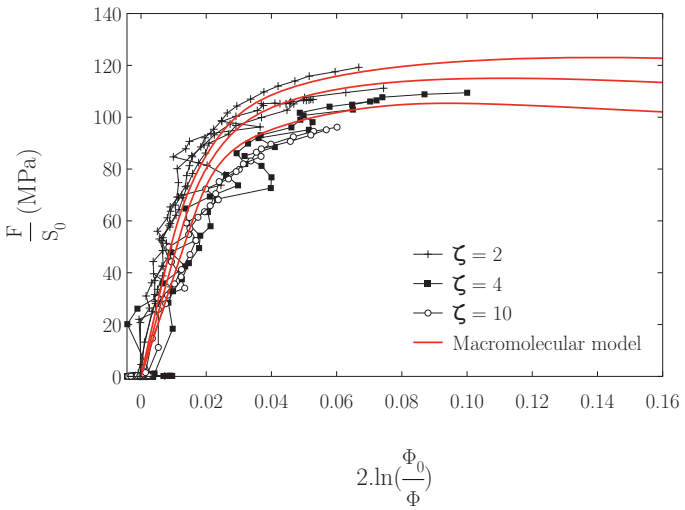

Fig. 18. Model verification for pressure sensitivity against experimental results taken at $T = 25°\text{C}$ and $\dot{\epsilon} = 10^{-1}/\text{s}$.

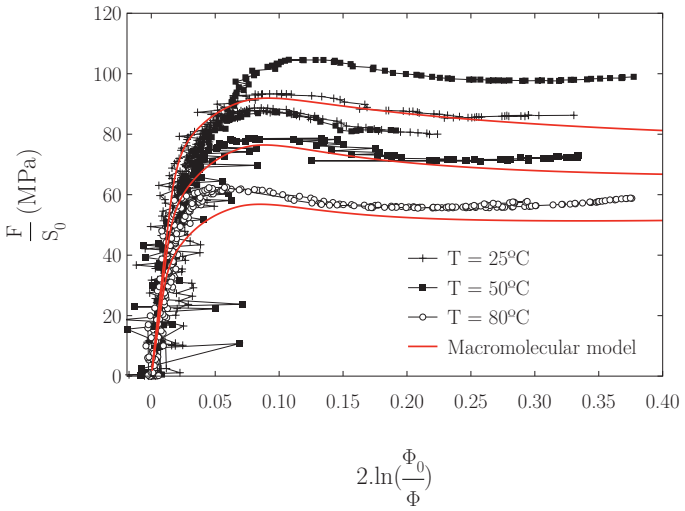

Fig. 19. Model verification for temperature sensitivity against experimental results taken at $\dot{\epsilon} = 10^{-3}$/s and $\zeta = 10$.

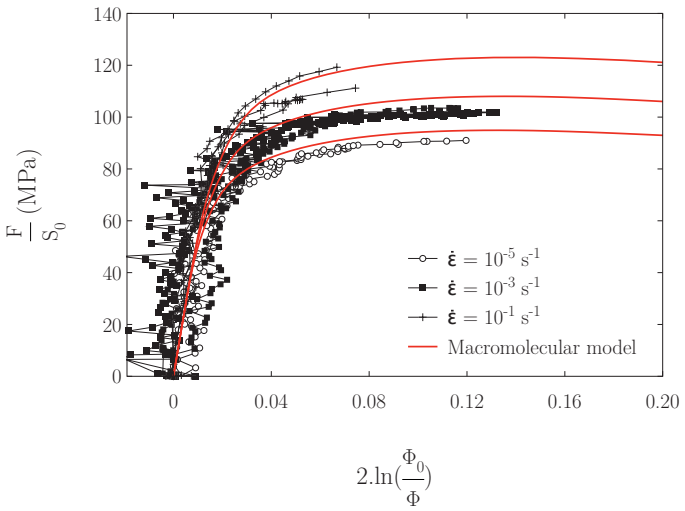

Fig. 20. Model verification for strain rate sensitivity against experimental results taken at $T = 25°\text{C}$ and $\zeta = 2$.

Table II. Material parameters used in the finite-element calculations, identified by Poulain [1].

Material parameter	Units	Description	Epoxy Epon 862
ρ	kg/m^3	mass density	1100
E_r	GPa	modulus at T_r	2.6
T_r	K	reference temperature	298
β	1/K	temperature dependence	0.0028
ν	—	Poisson's ratio	0.4
s_0/E	—	initial shear strength	45.8
s_1/s_0	—	pre-peak strength	1.2
s_2/s_0	—	saturation strength	1.1
h_1	MPa	pre-peak hardening	2994
h_2	MPa	rate of yield drop	896.6
$\bar{\epsilon}_p$	—	peak plastic strain	0.054
f	—		0.1
α	—	pressure-sensitivity	0.05
m	—	rate-sensitivity	0.5
$\dot{\epsilon}_0$	s^{-1}	rate-sensitivity	43000
A	1/K	rate-sensitivity	173.8
C^R	MPa	rubbery modulus	15
N	—	number of rigid links	7.4

CHAPTER IV

MECHANICS OF NOTCHED BARS

A. Introduction

Numerical simulations can provide insight into the complex stress and strain distributions that an amorphous polymer experiences during multi-axial loading conditions. However, these simulations, and the knowledge gained from them, are limited by the accuracy of the constitutive model used to define the behavior of the material. In chapter III, a physics based model for polymers has been presented which is capable of accounting for rate-, pressure-, and temperature-sensitive yielding, isotropic hardening before peak yield, intrinsic postyield softening, and rapid anisotropic hardening at large strains. Using the model's capabilities, the aim of this chapter is to investigate the stress triaxiality spatial distribution and evolution in the notched round bars presented in chapter II. The peculiar polymeric material response to various stress states is compared against a more common deformation behavior observed in materials following a power law hardening. Also, the effects of the specimens geometry on the stress triaxiality is investigated for various notch acuities. The results show that the stress triaxiality does not vary by the amount expected based on the finite element analyses that were used to design the experiments. The influence, of what was initially thought to be a minor change in the specimen geometry, is quite significant and strongly affects the stress state evolution.

B. Background

In order to evaluate the effects of the stress triaxiality on the strain to failure, it is necessary to perform different tests where the level of triaxiality can be varied. As mentioned previously, the classical tensile test on notch specimens is one of the most common ways to achieve this goal. The experimental work presented in chapter II was based on previous studies for ductile fracture in metals [14]. The dimensions of the specimens are shown in Fig. 5. The larger diameter Φ_{max} was originally specified to be 7 mm for all the bars, however, due to manufacturing constraints the specimens had to be machined from stock sheets of resin plates of 60.96×60.96×6.35 (mm) where 6.35 mm is the sheet thickness, therefore the original diameter had to be reduced to 5.8 mm.

The fracture locus of the material has been defined as a measure of fracture property (mean strain to failure) versus a measure of stress state (stress triaxiality ratio). To quantify the triaxiality of the stress state, a stress triaxiality ratio, τ, was defined in equation 2.2. When notched specimens are designed, in general, the goal is to minimize variations of the stress triaxiality ratio with deformation, so its effect on the fracture behavior can be quantified in a more controllable manner. This has been done extensively for power law hardening materials such as metals. Our experiment was designed following such guidelines (see chapter II). However polymers deformation behavior does not obey power laws. And therefore it is necessary to investigate the distribution of the stress triaxiality ratio corresponding to the original specimen geometry ($\Phi_{max} = 7$ mm), using a material model that follows more realistically the deformation behavior of polymers. Also it is important to find out how the modification in the specimens larger diameter, Φ_{max}, would impact the results.

The power law hardening law used is a Ramberg-Osgood model define as follows:

$$E\epsilon = \sigma + \alpha \left(\frac{|\sigma|}{\sigma_0} \right)^{n-1} \sigma \tag{4.1}$$

where E is the Young´ s modulus, α is the yield offset, σ_0 is the yield stress and n is the hardening exponent with $n > 1$. For a particular set of testing conditions (temperature and strain rate), using the corresponding experimental stress-strain response of smooth bars, the power law material parameters were determined by fitting a curve onto the smooth bar response, see appendix A Fig 41. Table III summarizes the value of the material parameters used for the case of $T = 25°\text{C}$ and $\dot{\epsilon} = 10^{-3}/s$.

Table III. Material parameters used in the power law finite-element calculations.

Material parameter	Units	Description	Epoxy Epon 862
E	GPa	modulus	2.6
α	-	yield offset	0.02
σ_0	MPa	yield stress	50
n	-	hardening exponent	9.5

C. Effects induced by the material model

The evolution of the stress triaxiality ratio with respect to the deformation along the specimen minimum cross-section is show in Fig. 21 for all notch acuities. The variations of triaxiality versus the mean strain are compared when two different material deformation models are used in the numerical simulations. First, it is found that for a power law hardening material, the stress triaxiality ratio increases as the mean strain increases at the specimen's center, Fig. 21 (a), and the opposite trend is observed at

the specimen's notch root, Fig. 21 (b), where triaxiality decreases as the mean strain increases. In both cases, center and notch root, triaxiality evolves in a rather smooth manner. Now, when the material follows a more complex and realistic constitutive model accounting for isotropic hardening before peak yield, intrinsic postyield softening, and rapid anisotropic hardening at large strains, triaxiality variations are no longer smooth. For all notch acuities, at the specimen's center, after some increase, the stress triaxiality ratio reaches a maximum and then decreases towards what seems to be a common value of $\tau \approx 0.3$ for all notch acuities which corresponds to triaxiality ratio of a smooth bar. A similar observation can be made at the specimen's notch root. In other words, at large strains, the stress state in the specimen section of minimum diameter seems to become uniaxial.

In order to further understand what is going on at larger strains, let's now look at deformed configurations of the finite element specimen models. Fig. 22 shows the simulated contour evolution of the effective plastic strain for a power hardening material, Fig. 22 (a), and a more realistic polymer behavior using the macromolecular model, Fig. 22 (b). In the macromolecular model case, a neck seems to be developing in the notch region along with some elongation of the material in the mid-section. In contrast, for the case of using a power law, the overall geometry of the notch is maintained. In addition, the evolution of the stress triaxiality contour in Fig. 23 shows a significant difference between both cases. As observed in Fig. 21, in the specimen mid-section, for the simulation using the macromolecular model, the stress triaxiality ratio at large strain ($\bar{\epsilon} = 0.85$) is approximately equal to the one of a smooth bar. Also, triaxiality seems to be building up in the region below the specimen mid-section, whereas it remains concentrated in the center of the specimen for the power law case.

(a)

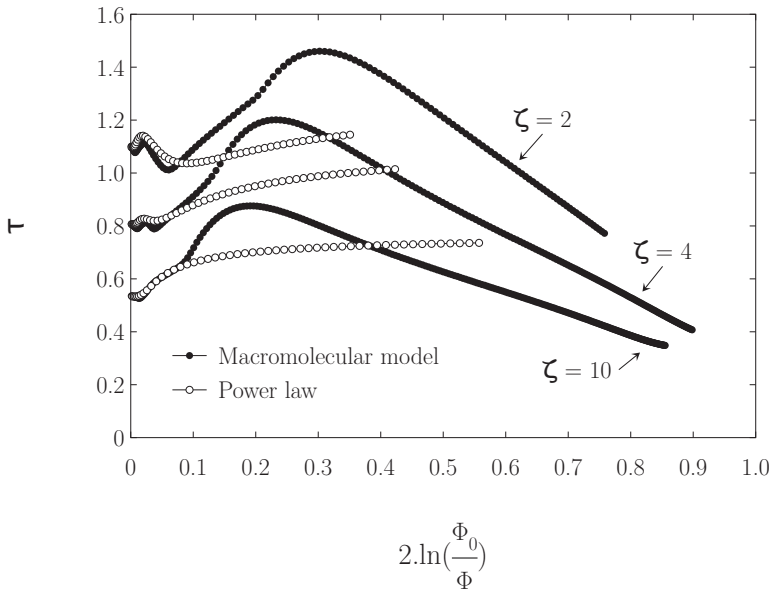

(b)

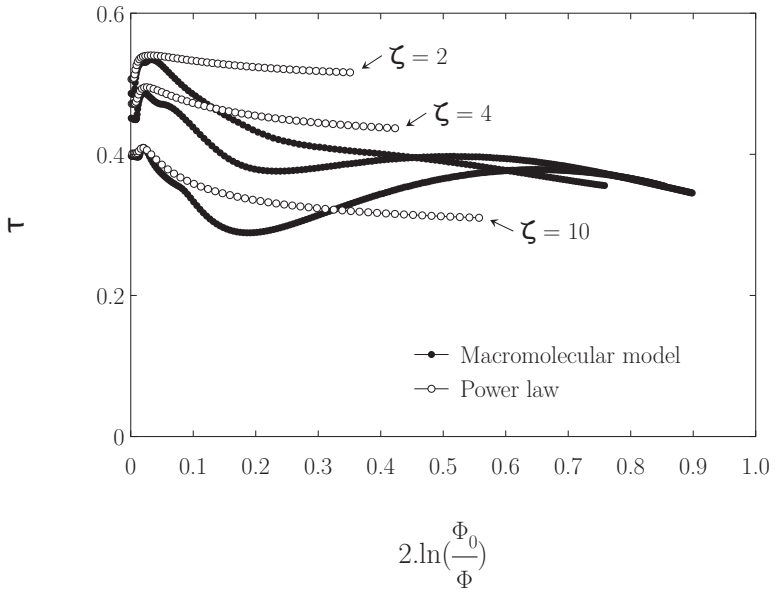

Fig. 21. Stress triaxiality ratio versus minimal cross-section mean strain at $T = 25°\mathrm{C}$ and $\dot{\epsilon} = 10^{-3}/s$ for various levels of notch acuity. This figure compares different material models and corresponds to the evolution of the stress triaxiality taken at, (a) the specimen's center, (b) the specimen's notch root. (original specimen geometry)

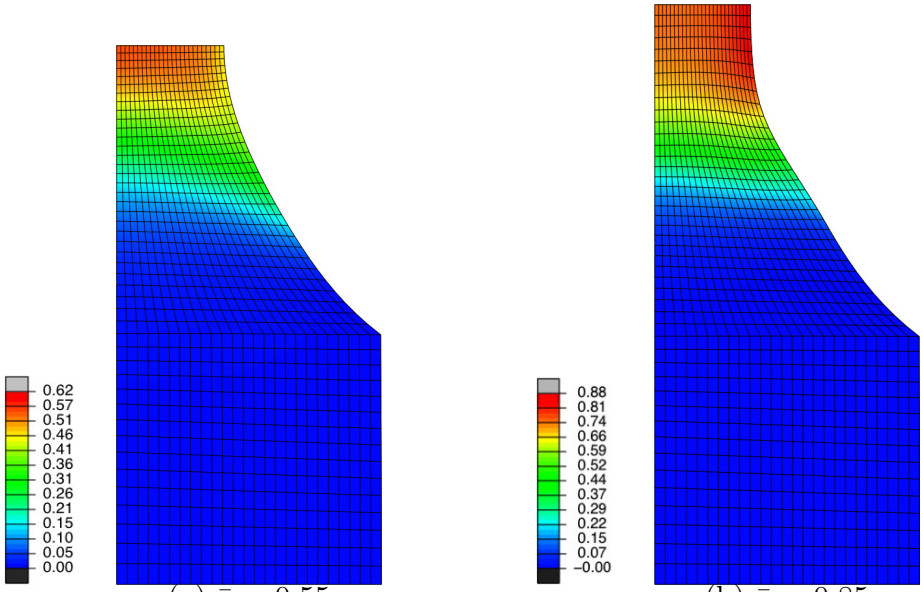

(a) $\bar{\epsilon} = 0.55$ (b) $\bar{\epsilon} = 0.85$

Fig. 22. Evolution of effective plastic strain for (a) power law, (b) macromolecular model.

D. Effects induced by the specimen geometry

Due to manufacturing constraints, the specimen larger diameter, Φ_{max}, had to be reduced from 7 to 5.8 mm (see chapter II). In order to gain knowledge on how this design change might have impacted the results, numerical simulations using the macromolecular model have been run for both, the modified and original specimen geometry. Fig. 24 shows the evolution of the stress triaxiality along the specimen's minimum cross-section where r is its radius ($r = 0$ and $r = 1.9$ mm, corresponds to the specimen's center and notch root respectively). The results are extracted for fixed levels of strain, at the onset of deformation $\bar{\epsilon} = 0$, Fig. 24 (a), and at $\bar{\epsilon} = 0.4$, Fig. 24 (b). The first observation is that the impact of the change in geometry is clearly dependent on the stress triaxiality levels induced by the notch radius. For $\zeta = 2$, there is a significant reduction in the range of triaxiality, whereas for $\zeta = 10$, the change

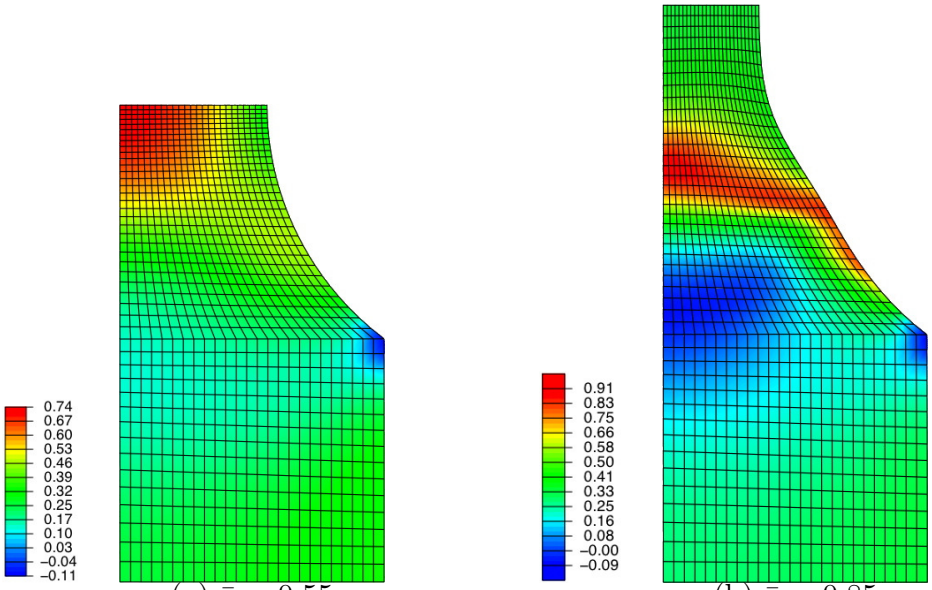

(a) $\bar{\epsilon} = 0.55$ (b) $\bar{\epsilon} = 0.85$

Fig. 23. Evolution of the stress triaxiality ratio for (a) power law, (b) macromolecular model.

in geometry has almost no influence at all on the simulations results. Moreover, its impact seems to wear off as the location of interest goes from the center ($r = 0$) to the notch root ($r = 1.9$) of the specimen. Last, when comparing Fig. 25 (a) and (b), which depicts the evolution of the triaxiality ratio throughout deformation captured at the specimen's center and notch root. It is clear that the influence of the geometry modification is diminished as the deformation increases. In addition, the range of stress triaxiality is greatly reduced by this change. In order to remedy this effect, instead of only reducing the diameter Φ_{max}, the others dimensions could have been also reduced by a proportional amount.

(a)

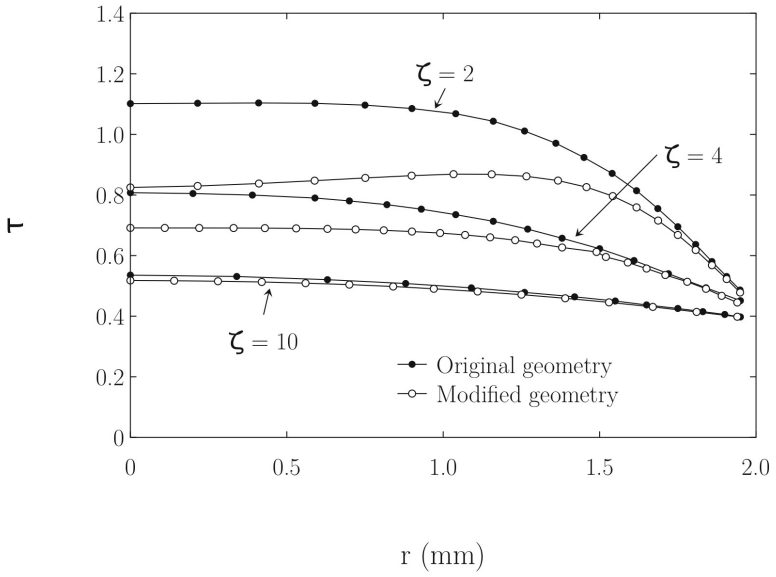

(b)

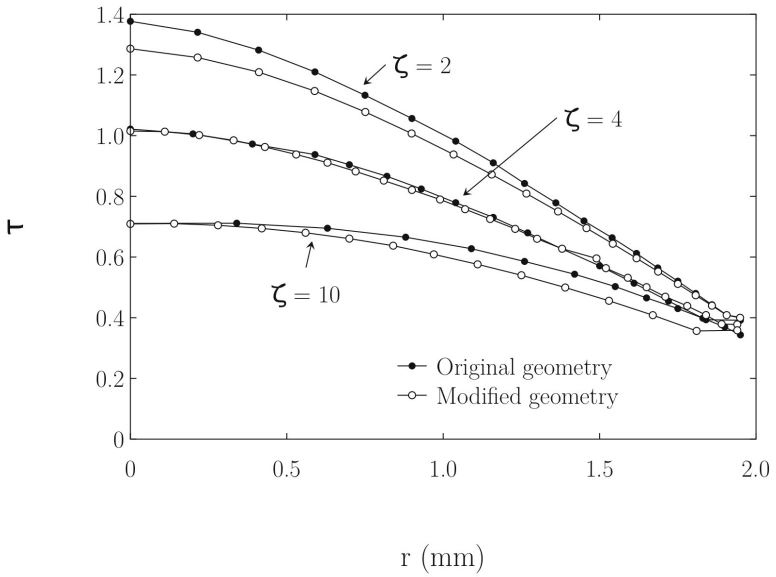

Fig. 24. Stress triaxiality ratio versus radius along the minimal cross-section at $T = 25°\text{C}$ and $\dot{\epsilon} = 10^{-3}/s$ for various levels of notch acuity taken at (a) $\bar{\epsilon} = 0$, (b) $\bar{\epsilon} = 0.4$.

(a)

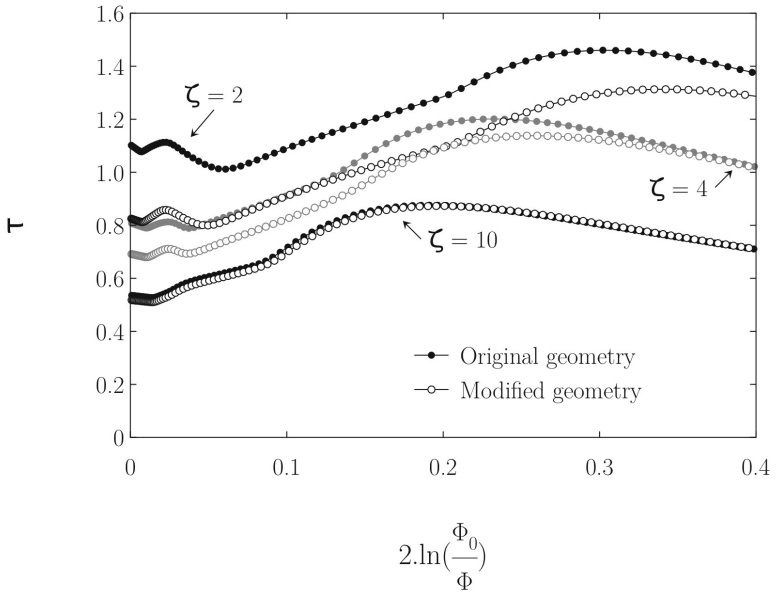

(b)

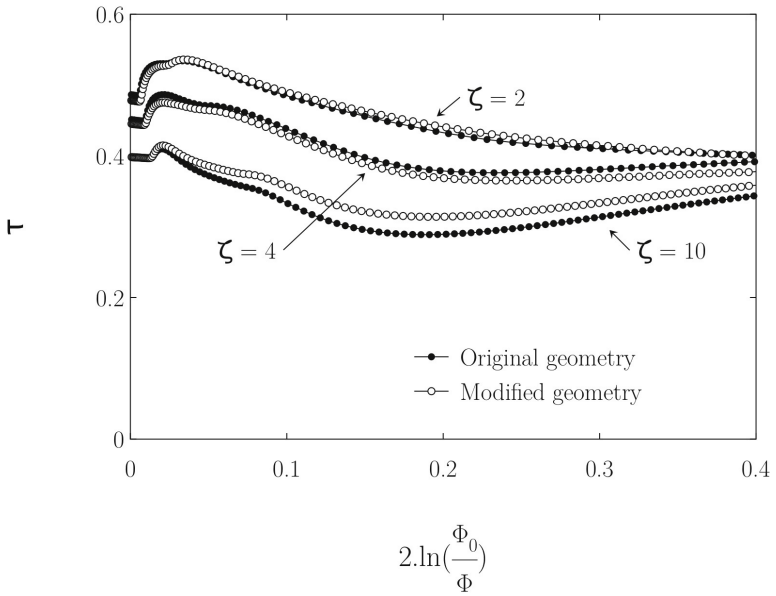

Fig. 25. Stress triaxiality ratio versus minimal cross-section mean strain at $T = 25°\mathrm{C}$ and $\dot{\epsilon} = 10^{-3}/s$ for various levels of notch acuity taken at (a) the specimen's center, (b) the specimen's notch root.

E. Conclusion

A series of tensile tests on epoxy round notched bars were carried out in order to provide clues on the dependence of the fracture behavior upon the stress triaxiality. Numerical simulations using Abaqus UMAT have been performed using a material model that follows realistically the peculiar deformation behavior of amorphous polymers. The correlation of experimental and numerical results shows a very good agreement between the two. Despite lack of literature on the subject, there are experimental works that have shown a clear dependency between the stress state and the fracture behavior of polymers in general. It has been shown that care should be taken when trying to formulate a fracture locus applicable to amorphous polymers. Indeed, the design of the specimens, which was based on previous work on ductile fracture for metals, caused strong temporal and spatial variations of the stress triaxiality. However, the triaxiality levels induced by the notch radii of the specimens can be easily distinguished. Also, what was initially thought to be a minor change in the specimen geometry turned out to reduce significantly the range of stress triaxiality achieved by the three notch radii considered in this work.

CHAPTER V

DEVELOPMENT OF A FRACTURE MODEL

A. Background

1. When does fracture initiate?

As mentioned in chapter II, from the tensile experiments on notched bars, it is impossible to differentiate when damage initiates ($\bar{\epsilon}_i$) from macroscopic fracture ($\bar{\epsilon}_f$) since the crack propagation stage is so sudden. Therefore, levels of mean strain, at which macroscopic fracture occurs, are considered to be the moment when fracture initiates. From the experimental force/radial-displacement curves, the radial displacements to fracture were obtained from the sudden drop of the curves, then the corresponding mean strains were determined. We shall refer to these levels of strain as the moment when cracking initiates, defined as $\bar{\epsilon}_i$. Also, up to four realizations of each test condition (type of notch, temperature and strain rate) were obtained during the experiments. Significant scatter was observed for certain conditions of temperature, strain rate and notch acuity. Therefore, for the sake of quantifying the strain levels at which complete specimen failure was observed, $\bar{\epsilon}_i$, for a given set of test conditions (ζ, T and $\dot{\epsilon}$), the average over all realizations was considered. In Fig. 26 the scatter is illustrated by the colored zone which is bounded by the minimum and maximum mean strain to failure observed over 4 realizations performed at $T = 25°\text{C}$ and $\dot{\epsilon} = 10^{-1}/\text{s}$ for a notch acuity of $\zeta = 2$. The vertical red dotted line corresponds to the average value defined above. For the remainder of this chapter, all the results from the numerical simulations were calibrated at strain levels up to this averaged $\bar{\epsilon}_i$, for a given

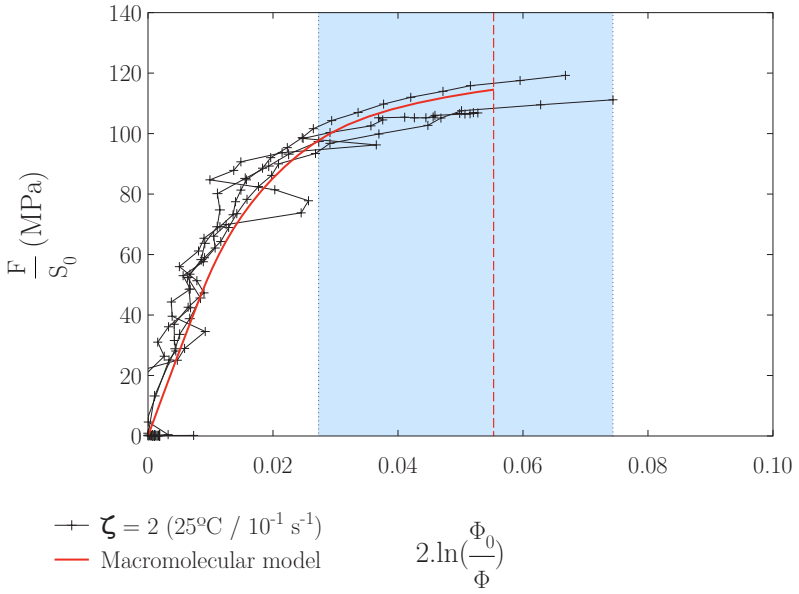

Fig. 26. Normalized load versus minimal cross-section mean strain at $T = 25°\text{C}$ and $\dot{\epsilon} = 10^{-1}/\text{s}$ for a notch acuity of $\zeta = 2$.

set of test conditions.

2. Where does fracture initiate?

In Fig. 14, 15 and 16 from chapter II–2, pictures of the fracture surfaces of each notched specimens were taken postmortem using a low powered optical microscope. Observations of the fracture surfaces have shown that the location where fracture initiates varies depending on the levels of stress triaxiality induced by the notch acuity. As the stress triaxiality increases in intensity, the location of the onset of fracture switches from a region near the specimen's center to the notch root vicinity. In order to further understand what mechanical quantities are behind these observations, let's look at Fig. 27 which depicts the evolution of the stress triaxiality ratio, τ, along the specimen's minimum cross-section for various notch acuities. Where r is the

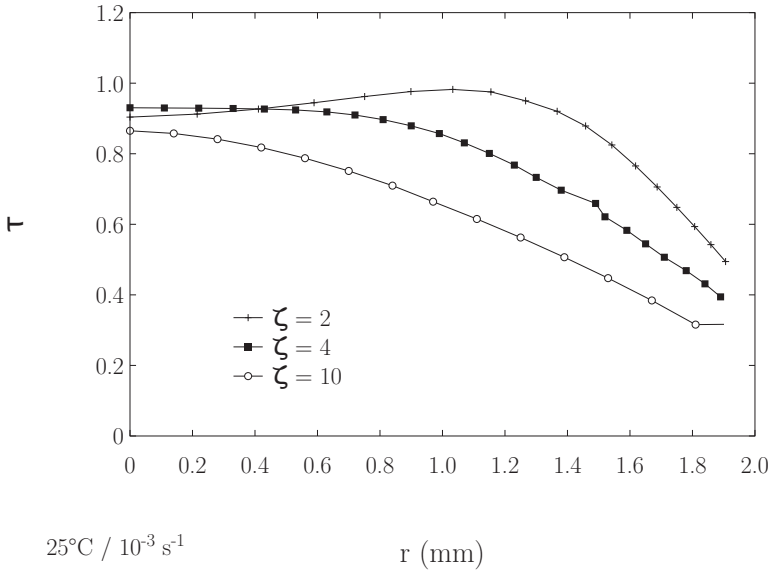

Fig. 27. Stress triaxiality ratio versus radius along the minimal cross-section at $T = 25°\text{C}$ and $\dot{\epsilon} = 10^{-3}/s$ for various levels of notch acuity captured at $\bar{\epsilon}_i$

specimen's minimum cross-section radius ($r = 0$ and $r = 1.9$ mm, corresponds to the specimen's center and notch root respectively). The results are extracted at $\bar{\epsilon}_i$, defined earlier.

From the fracture surfaces observations, a more acute notch translates into a shift of the fracture initiation point towards the notch root. Now, looking at the curve corresponding to $\zeta = 2$, the stress triaxiality ratio reaches a peak for $r = 1$–1.2 mm whereas for $\zeta = 4$ and 10, the peak is reaches in the specimen's center. When comparing the fracture surfaces observed in Fig. 14 and 15 with this results, there seems to be a correlation between the peak stress triaxiality ratio and the actual location of fracture initiation.

Furthermore, similar observations can be made be looking at Fig. 28. Here, the evolution of various stresses is plotted against r (identically defined as earlier). σ_I

(a)

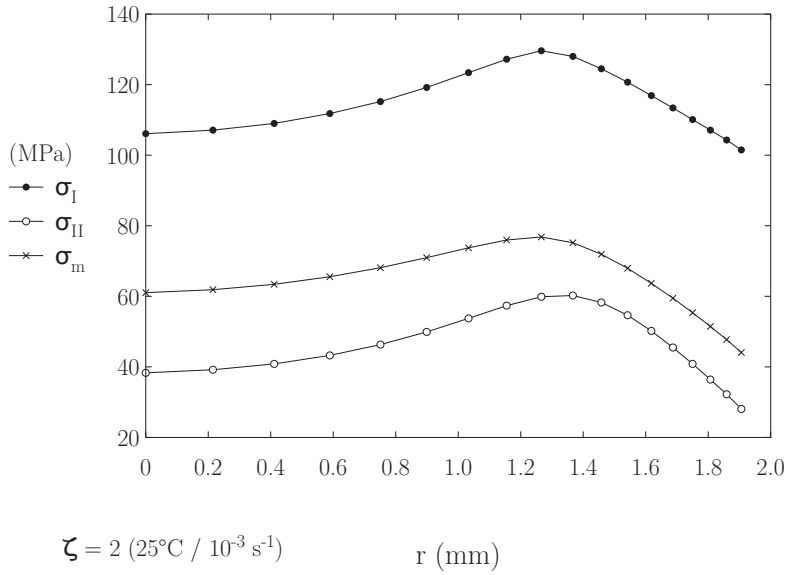

(b)

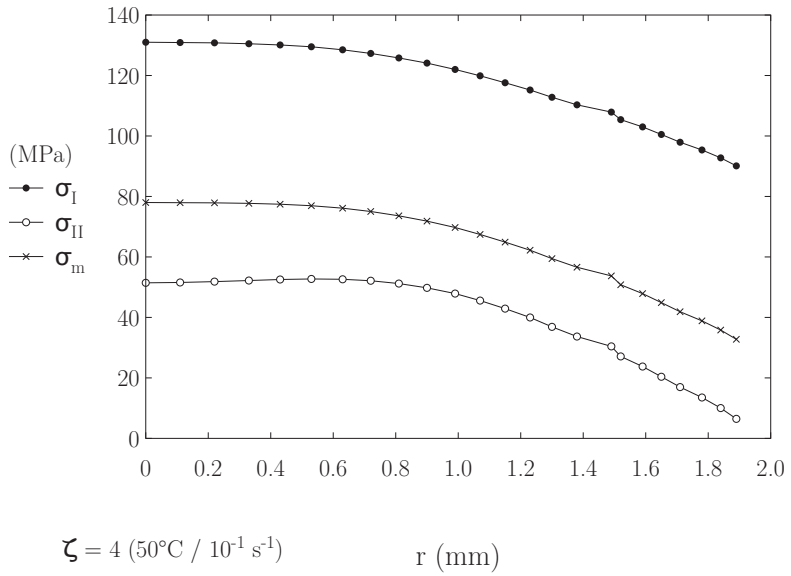

Fig. 28. Various stresses versus radius along the minimal cross-section captured at $\bar{\epsilon}_i$ with, (a) $\zeta = 2$, $T = 25°\text{C}$ and $\dot{\epsilon} = 10^{-3}/\text{s}$, (b) $\zeta = 4$, $T = 50°\text{C}$ and $\dot{\epsilon} = 10^{-1}/\text{s}$.

refers to the maximum principal stress, σ_{II}, the intermediate principal stress and σ_m, the mean stress. Fig. 28(a) and (b) are similar plots captured at different notch acuities, temperatures and strain rates. By comparing the two, it is clear that the maximum principal stress, for instance, is also correlated with the fracture initiation site. Its corresponding peak occurs at roughly $r \approx 1.2$ mm, in the same region as the peak stress triaxiality showed previously. Therefore, in the same regard as for the stress triaxiality ratio, there seems to be a correlation between the peak of the maximum principal stress and fracture initiation site.

B. Presentation of the model

The fracture initiation criterion is motivated by the collaborative work of many researchers over the past 40 years (see chapter I–D). Based on the experimental work on PMMA of Sternstein et al. [26, 27] and recently refined by Gearing et al. [29], the criterion is essentially empirical in nature and as such, it can be used to model cracking in a wide class of glassy polymers. Crack initiation is taken to occur when the maximum principal stress σ_I attains or exceeds a (positive) pressure-dependent critical value, σ_c, while the mean normal stress, $\sigma_{kk}/3$ is positive. The pressure dependence of σ_c is specified by

$$\sigma_I = \sigma_c(\sigma_{kk}) = c_1(T) + \frac{c_2(T)}{\sigma_{kk}} \tag{5.1}$$

where c_1 and c_2 are temperature-dependent material parameters. In order to determine their dependencies upon temperature, two levels of approximation are considered. The first being linear with $c_i = c_{i1}T + c_{i2}$ and the second being quadratic with $c_i = c_{i1}T^2 + c_{i2}T + c_{i3}$. c_1 and c_2 are calibrated in the next chapter on the experimental

data.

The constitutive relations (3.3)–(3.14) specify the plastic flow prior to damage initiation. Once damage occurs, these equations cease to be valid. One established mechanism for glassy amorphous polymer fracture is craze formation, as mentioned in chapter I–A, which is a major cause of fracture in thermoplastic polymers. Although, elements of the model based on polymer crazing presented in this work were motivated by physical arguments, it remains phenomenological in nature. As such, it can also be used to model fracture in thermosetting polymers. During the craze growth stage, the deformation is no longer homogenous and localized mode of inelastic deformation takes place. Therefore, once crazing has initiated, specific craze flow constitutive equations are prescribed. The magnitude and the direction of the initial plastic flow rule for the macromolecular model (3.3) must be modified with the following tensor p (new direction of the plastic flow) and $\dot{\bar{\epsilon}}$ (new magnitude of the plastic flow),

$$p = \hat{e}_I \otimes \hat{e}_I \quad and \quad \dot{\bar{\epsilon}} = \dot{\bar{\epsilon}}_0^{cr} \left(\frac{\sigma_I}{(1 - (\chi/\chi_c)^2) s_{cr}} \right)^{\frac{1}{m}} \tag{5.2}$$

where $\hat{e}_I$ is a unit vector defining the direction of the maximum principal stress, σ_I. χ_c is typically about 0.6. χ is a state variable representing craze induced damage, and varies between 0, at the onset of crazing, and $\chi_f = 1$ at zero stress. χ is meant to describe the volume fraction of active fibrils in the craze structure. Also, $\dot{\bar{\epsilon}}_0^{cr}$ is a reference parameter chosen to ensure continuity of the plastic stretching at the transition from shear flow to craze flow, the two major fracture mechanisms for amorphous glassy polymers. m and s_{cr} are additional material constants. The following evolution equation is adopted of χ:

$$\dot{\chi} = C(\chi_f - \chi)\dot{\bar{\epsilon}} \tag{5.3}$$

with χ_f defined above and C an additional material constant. One consequence of

this formulation is that the loss of stress bearing capacity is a natural outcome to the craze growth process.

C. Calibration of the initiation criterion

In chapter V–A, the time (strain level) and the location of fracture initiation have been defined. Therefore, for a given set test conditions, the following results have been captured at strain levels corresponding to the mean strain to initiation defined earlier, $\bar{\epsilon}_i$. In addition, all quantities of interest are extracted along the specimen's minimal cross-section at the location where the maximum principal stress is the highest, as shown in Fig. 28, which is defined as σ_I^{max} corresponding to the maximum principal stress taken at strain levels $\bar{\epsilon}_i$ and at the location where fracture is assumed to initiate. *As a side note, the material exhibits significant plastic deformation prior to macroscopic failure, and since plastic deformation is path dependent, the fracture locus itself is path dependent as well. In this work, the values of the mechanical quantities of interest are extracted at failure as explained above, however, an average over the deformation could have also been considered which would have accounted, to some extent, for the history of those quantities.*

Taking into account the simple form of the criterion (5.1), the calibration procedure for the material parameters c_1 and c_2 is rather straight forward. At fixed strain rate taken arbitrarily at $\dot{\epsilon} = 10^{-1}/s$. We begin by plotting the critical stress, σ_c with respect to $1/\sigma_{kk}$ as shown in Fig. 29. With $\sigma_c = \sigma_I^{max}$ (defined above).

Each dots in the figure correspond to a particular notch acuity (ζ) at room temperature. The error bars account for the scatter in the experimental data (see chapter V–A). Then plotting a linear fit corresponding to those 3 points yields a sim-

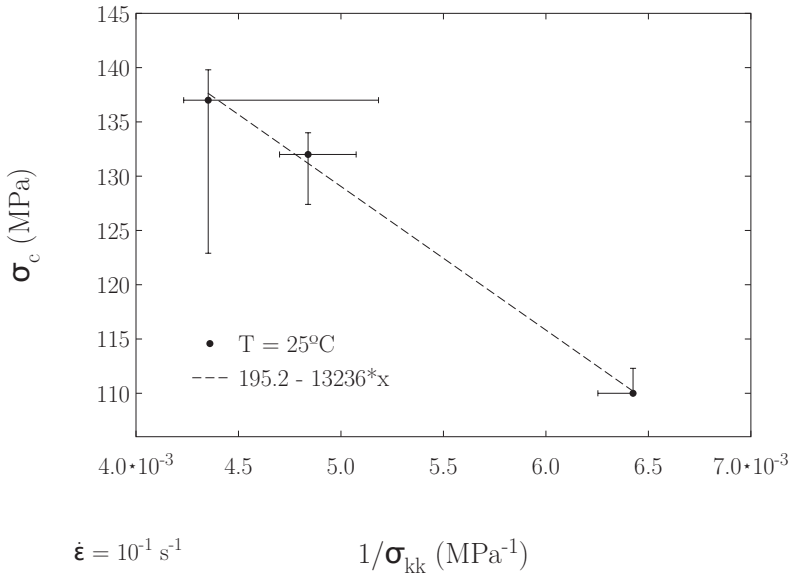

Fig. 29. Critical stress σ_c versus $1/\sigma_{kk}$ at $T = 25°\text{C}$ and $\dot{\epsilon} = 10^{-1}/s$. The dotted black line correspond to a linear fit with equation $\sigma_c = 195.2 - 13236(1/\sigma_{kk})$.

Table IV. Material parameters.

T (°C)	c_1 (MPa)	c_2 (MPa^2)
25	195.2	-13236
50	201.3	-16528
80	128.1	-4501

ple linear equation where the intercept corresponds to the c_1 value for that particular temperature (25°C) and strain rate (10^{-1}/s). Similarly, the slope corresponds to the c_2 value. Finally, reiterating the same process at temperatures of 50 and 80°C, while keeping $\dot{\epsilon} = 10^{-1}/s$, yields a set of c_1 and c_2 at each temperature as summarized in Table IV. The temperature dependency of c_1 and c_2 can be simply determined from Table IV by plotting them with respect to the temperature (T).

D. Results and discussion

The calibration procedure was carried out for a strain rate of 10^{-1}/s. In order to verify the predictive capabilities of the model, it is necessary to test it against different conditions of strain rates. Fig. 30 shows the error for all test conditions (ζ, T and $\dot{\epsilon}$) induced by the calibrated criterion using both, a linear, Fig. 30(a) and a quadratic approximation, Fig. 30(b). The error is defined as

$$Error = \frac{\sigma_c^{model} - \sigma_c^{exp.}}{\sigma_c^{exp.}} \tag{5.4}$$

where σ_c^{model} is the critical stress generated by the calibrated initiation criterion (5.1) and $\sigma_c^{exp.}$ is σ_I^{max} which was defined earlier using an experimental/numerical approach. From Fig. 30, it is clear that for a strain rate of 10^{-1}/s (used for calibration) the error, from both levels of approximation, is minimum.

However, for the linear approximation, the maximum error increases significantly as the strain rate decreases from its calibrated value. For the quadratic approximation, which yields better results, the maximum error seems to be contained at a constant level ($\approx 20\%$) as the strain rate changes. Also, in both cases, the model predictions are almost consistently higher than the reference ($\sigma_c^{exp.}$) which from a conservative

(a)

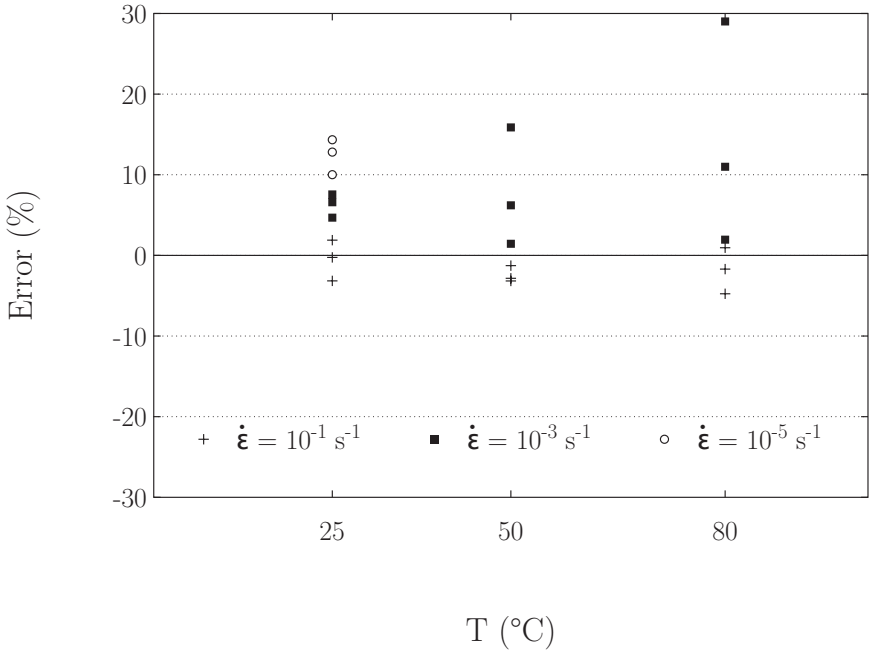

(b)

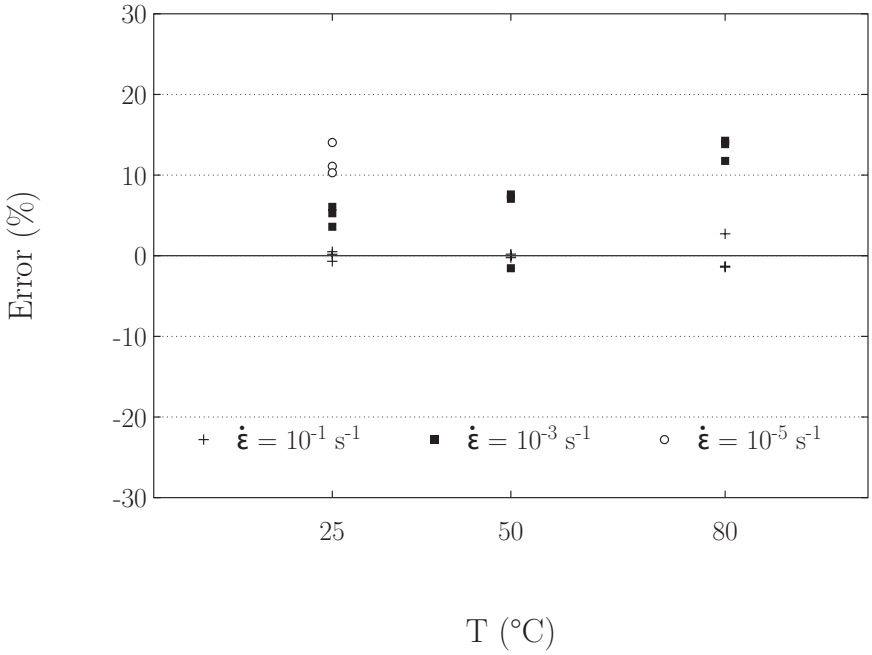

Fig. 30. Error induced by the calibrated criterion defined in equation 5.4
(a) Linear approximation, (b) Quadratic approximation.

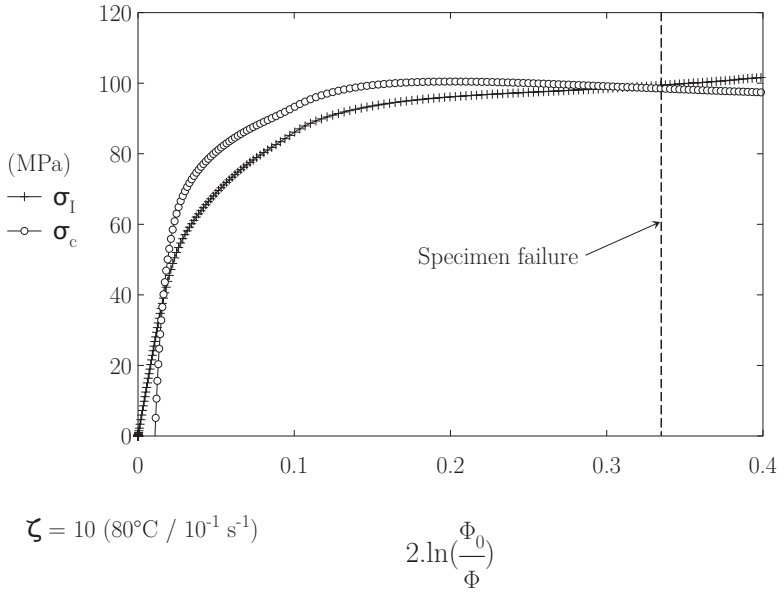

Fig. 31. Maximum principal stress and critical stress versus minimal cross-section mean strain for $\zeta = 10$, $T = 80°\text{C}$ and $\dot{\epsilon} = 10^{-1}/\text{s}$.

stand point is not ideal.

The criterion (5.1) means that when the maximum principal stress σ_I reaches a critical value σ_c, fracture initiates. Fig. 31 illustrates how well the criterion is able to predict fracture. When the curve corresponding to the maximum principal crosses the one corresponding to the critical stress, fracture is expected to initiate. The curve representing σ_c has been generated using the calibrated criterion (5.1). In this case, the prediction capabilities of the criterion are in very good agreement with the observed mean strain to failure, which is represented by the vertical dotted line. Such a good agreement is expected since the criterion has been calibrated at $\dot{\epsilon} = 10^{-1}/s$ and Fig. 31 corresponds simulations run at the same strain rate. However, when the criterion performances are compared at different strain rate such as $\dot{\epsilon} = 10^{-3}/s$, see Fig. 32, fracture initiation is predicted at a level of mean strain of roughly 0.5 whereas the experimentally observed fracture initiation, $\bar{\epsilon}_i$, occurs at about 0.35.

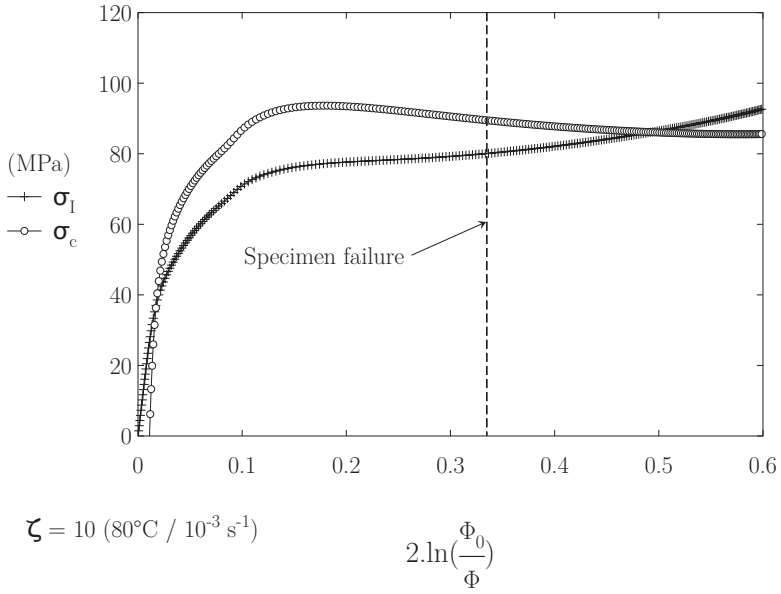

Fig. 32. Maximum principal stress and critical stress versus minimal cross-section mean strain for $\zeta = 10$, $T = 80°\text{C}$ and $\dot{\epsilon} = 10^{-3}/\text{s}$.

Also, in both figures (31 and 32), the curve representing the maximum principal stress intersects the critical stress curve twice. The first intersection being consistently in the region corresponding to the elastic regime. Therefore, when the criterion is to be implemented into a finite element code, care should be taken so fracture is not predicted prematurely.

The initiation criterion presented in this chapter has the main advantage of being simple to implement with a straightforward procedure to identify the two temperature dependent material parameters. It is also able to account for pressure sensitivity via the term σ_{kk}. Results have shown that in terms of accuracy, the criterion yields predictions that tends to worsen as the strain rate changes further away from the calibrated conditions. However, we have seen that the experimental data presented earlier shows significant scatter across the range of notch acuities, temperatures and strain rates used in this work. All the simulated results have been extracted at an

average value of $\bar{\epsilon}_i$, thus, part of the prediction errors observed from the criterion (5.1) may come from the experimental scatter. Moreover, the rationale for the notched bar tensile tests was to vary, in a controlled manner, the stress triaxiality and thus to calibrate the fracture criterion, which is pressure sensitive. However, it has been shown in chapter IV that the stress triaxiality not only strongly varies but the range in triaxiality achieved by the notched bars is narrower than what was initially expected, mostly due to the change in the specimen that occurs during the manufacturing process. With those issues in mind, the predictions are still within acceptable range making them meaningful for potential applications involving fracture of amorphous polymers where the pressure dependence must be accounted for.

CHAPTER VI

AGING OF EPON 862

A. Introduction

As described in chapter I, aging processes are conventionally separated into physical aging and chemical aging. The former is essentially a continued curing process in case of a thermosetting polymer where the polymer specific volume goes slowly with time from a non-equilibrium state initially to an equilibrium state. The chemical aging such as thermal degradation or photo-oxidation, on the other hand, causes permanent changes to the molecular structure.

In the experiments reported in chapter II as well as in the modeling of chapters III and V, it was tacitly assumed that the material properties are not altered and are time-invariant during the tests or simulations. This is usually a good assumption when the initial age of the material exceeds the experimental or simulation time. However, for long-term loading conditions or under circumstances where accelerated aging may occur, e.g., at high temperatures, the above assumption no longer holds [42]. By way of consequence, the material properties are expected to change during the experiment, and the simulation must rely on a model that accounts for the associated change in material parameters.

In the experimental plan presented in chapter II, investigation of the effects of aging on the deformation and fracture behavior of epoxy Epon862 were also carried out. Similarly to the experiments performed on unaged specimens, aged notched bars were tested in tension at various temperatures (25°C, 50°C and 80°C) at different

levels of nominal strain-rate (10^{-5}/s, 10^{-3}/s and 10^{-1}/s). Up to four (4) realizations of each test condition (type of notch, temperature and strain rate) were obtained. Physical aging was achieved by subjecting the specimens to isothermal aging at 121°C (12°C above the epoxy's glass transition temperature) for over 1750 h. The specimens were placed in a thermal chamber for 90 min each day for an average of three days a week over a six months period. For each cycle, a maximum temperature in the chamber of 121°C (250°F) was reached. The following chapter presents the results obtained from the tensile experiments on aged notched round bars.

B. Effects on the fracture behavior

As mentioned in this thesis introduction, very little work as been reported in the literature about the effect of aging on the fracture response for amorphous polymers. One investigation from Kong [3] has shown that as physical aging proceeds, the fracture behavior of the epoxy polymer investigated is clearly affected with a decrease in its ultimate mechanical properties such as its ultimate strength and its strain to failure. The material fractures in a more brittle fashion with aging (see Fig. 3). Similar findings are illustrated in Fig. 33 where the experimental data for unaged and aged specimens captured at $T = 80$°C and $\dot{\epsilon} = 10^{-3}$/s for various levels of triaxiality are compared. Fig. 33 (a) and (b) corresponds respectively to the sharpest notch acuity ($\zeta = 2$) and the shallowest notch acuity ($\zeta = 10$). The first observation is that the trend of a decreasing ultimate tensile strength reported by Kong is not only absent but the trend is reversed. To some extent, the aged specimens show an increase of the ultimate tensile strength compare to the unaged ones. This was also observed in smooth bars, where aged notched bars generally exhibit higher strength

than the corresponding unaged specimens [1]. This increase of strength with aging seems to be more pronounced for conditions favoring a lower stress, such as a lower stress triaxiality (comparing Fig. 33 (a) and (b)), a lower strain rate or a higher temperature; see details in Appendix B for more results. Second observation, the strain to failure is significantly affected by aging as observed by Kong. On average, the strains to failure for the aged specimens are roughly half of the one observed for the corresponding unaged specimens.

Figure 34 depicts the effect of notch acuity on the load–deformation response of an aged specimen. The sample results are shown for T = 25°C and $\dot{\epsilon} = 10^{-3}$/s. The load is higher in a bar with a sharp notch ($\zeta = 2$) than in one with a shallow notch ($\zeta = 10$), as expected.

In chapter II–C, it was shown that the mean strain to failure was strongly affected by the level of stress triaxiality, defined as τ (2.2). The results indicated a consistent trend for a decreasing ductility with increasing τ, the strains to failure being smaller in bars with a sharp notch. This trend was summarized in Fig. 12 which depicts examples of the so-called fracture loci. Following the same line of thought, a similar fracture locus is plotted in Fig. 35 where this time, the loci for unaged and aged specimens are compared at fixed testing conditions of $\dot{\epsilon} = 10^{-3}$/s, $T = 25$°C in Fig. 35 (a) and $T = 25$°C in Fig. 35 (b). Note the scatter in the values of the mean strain to failure around the average value (indicated by a point). While the trend of decreasing strain to failure with aging, mentioned earlier, is also apparent here, more interestingly, the decrease of ductility with increasing stress triaxiality τ appears to a lesser extent for the aged case. The difference in strain to failures going from one level of triaxiality to another is not as significant as for the unaged results. By comparing Fig. 35 (a) and (b), it appears that the temperature has a significant influence on the response of the aged specimens. While for the case of $T = 25$°C

(a)

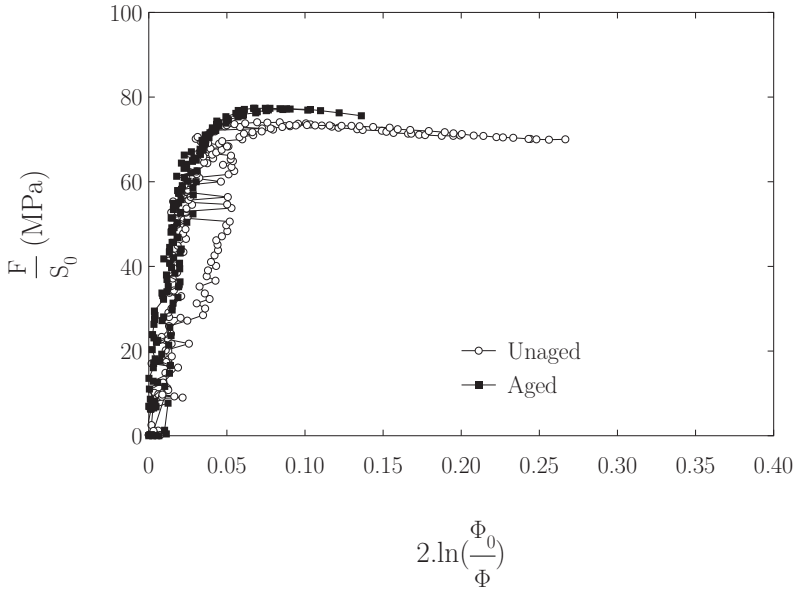

(b)

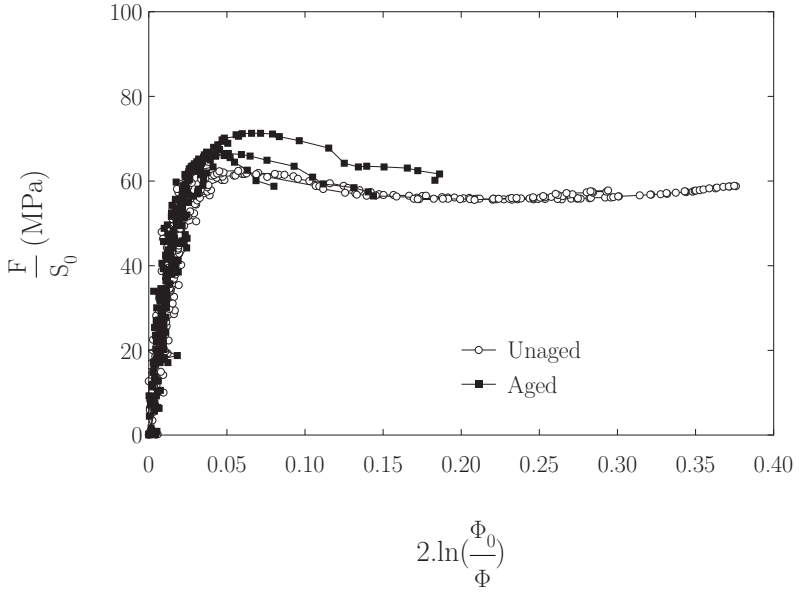

Fig. 33. Normalized load versus minimal cross-section mean strain for aged specimens captured at $T = 80°\text{C}$ and $\dot{\epsilon} = 10^{-3}/\text{s}$ for various levels of triaxiality, (a) $\zeta = 2$ (b) $\zeta = 10$.

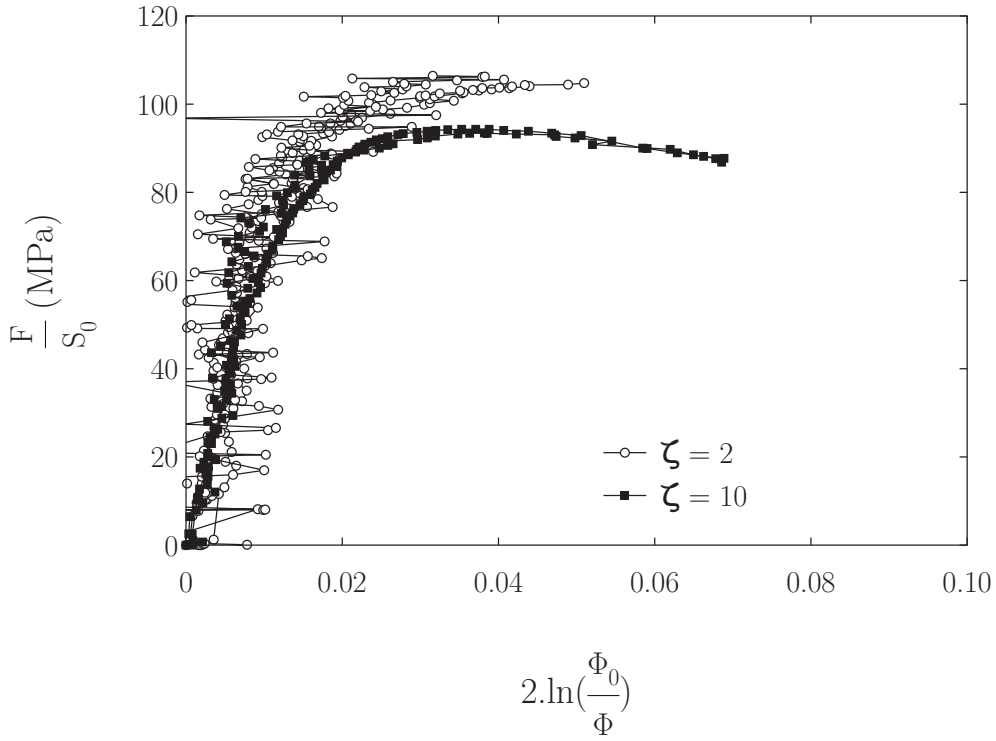

Fig. 34. Normalized load versus minimal cross-section mean strain for aged specimens captured at $T = 25°\text{C}$ and $\dot{\epsilon} = 10^{-3}/\text{s}$.

the difference between unaged and aged is rather small, for the case of $T = 80°C$ the fracture response of the aged specimens is consistently more brittle for a given level of triaxiality. Moreover, the impact of aging on the strain to failure seems to be decreasing with an increasing level of stress triaxiality. For instance, by comparing the average value of the strain to failure (plotted with an open circle and a full black circle for the unaged and aged results respectively) for the sharpest notch acuity (τ between 1.0 and 1.1) with the shallowest one (τ between 0.6 and 0.7), it is appears that the impact of aging is almost inexistant for the sharpest case. In contrast, the impact is significant for the shallowest notch acuity. Even the influence of aging on the fracture behavior seems to be dependent on the stress state.

One possible explanation for this observed phenomenon could be explained as follows. Physical aging effects on thermosetting polymers is essentially a continued curing process which rendered a more fully cross-link network. In other words, aged thermosets have a higher cross-link density, which generally tends to a stiffer material response. The cross-link density restricts the polymer network from deforming under applied load. When the levels of stress triaxiality are increased, on a molecular level, it leads to a rearrangement of molecular orientation and "opening up" of free volume, which ultimately facilitate molecular orientation. Easier to move means less stress is required for this orientation process. Therefore, effects of aging are canceled or limited by a greater mobility induced by a highly triaxial stress state.

C. Conclusion

One of the main objectives from the aged notched bar experiment was to investigate the effect of aging on the strain to failure. Major findings were established in that

(a)

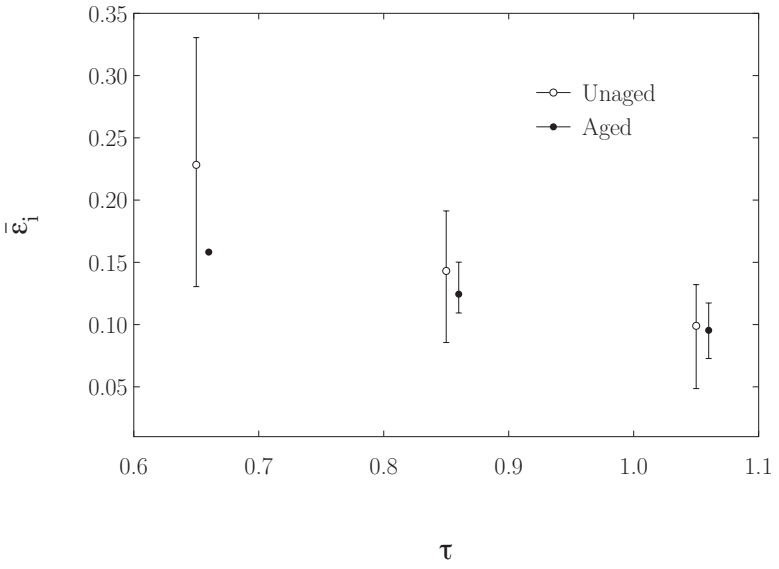

(b)

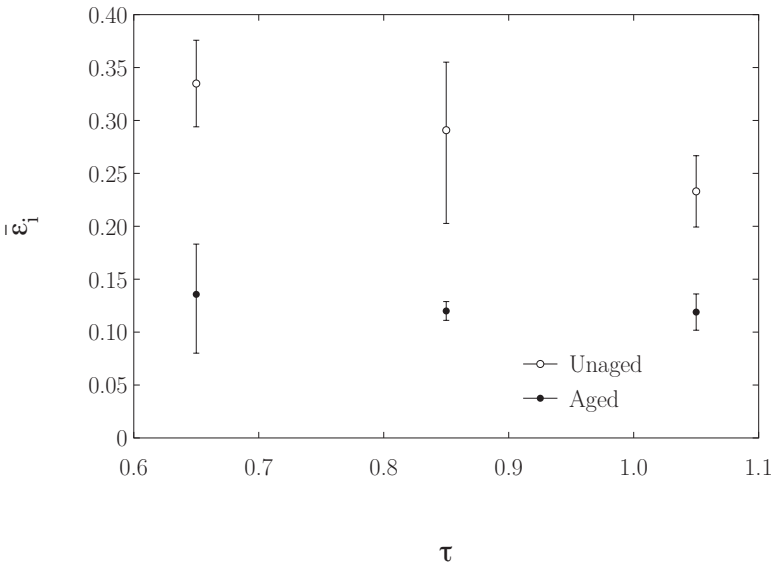

Fig. 35. Minimal cross-section mean strain to fracture versus triaxiality ratio captured at $\dot{\epsilon} = 10^{-3}$/s for unaged and aged specimens, (a) $T = 25°$C (b) $T = 80°$C.

regard. The following summarized what has been shown in this chapter. Additional results can be found in Appendix B.

- While the effect of aging on tensile strength is moderate, its effect seems to be more pronounced for conditions favoring more ductile conditions, such as a lower level of stress triaxiality.

- The strain to failure is significantly affected by aging. Aged specimens consistently exhibit a lower strain to failure compared to there unaged counterparts, regardless of the conditions of temperature, strain rate and notch acuity.

- As expected from unaged tests, the results indicated a consistent trend for a decreasing ductility with increasing τ, the strains to failure being smaller in bars with a sharp notch. However, the decrease of ductility with increasing triaxiality levels appears to a lesser extent for the aged specimens. The fracture locus seems to be flattened.

- Extent of the influence of aging on the fracture behavior seems to be strongly correlated with the temperature. A higher testing temperature increases the influence of aging on the strain to failure which occurs in a more brittle manner.

CHAPTER VII

CONCLUSION

In this research, a comprehensive experimental plan aiming to shed light on key aspects of amorphous polymers fracture behavior has been introduced in chapter II. A series of tensile tests on epoxy round notched bars were carried out in order to provide clues on the dependence of the fracture behavior upon the stress triaxiality. Using state-of-the-art non-contact digital image correlation measurement technique, the mechanical quantities of interest were extracted in order to understand how the polymer fracture behavior responds when subjected to various levels of stress triaxiality induced by the three notch radii considered in this work. It has been shown that the material is strongly sensitive to the stress state. A fracture locus was defined as a measure of fracture property versus a measure of stress state where the mean strain to failure and the stress triaxiality ratio were chosen to construct the fracture locus. Experimental results have made clear that a consistent trend exists with a decreasing material ductility as the stress triaxiality ratio increases. These types of results have been reported extensively in the literature for ductile fracture of metals giving the wealth of experimental data available on the subject. However, little is known to date on how amorphous polymeric materials fracture when subjected to multi-axial stress states. In addition, analyses of the fracture surfaces have revealed a strong correlation between the levels of triaxiality with the actual location site where fracture initiates. For highly triaxial conditions, the initiation site appeared to be systematically located in a region close to the specimen's notch root whereas for less

triaxial condition of stress, initiation was observed mostly at the specimen's center.

The underlying hypothesis was that the amount of hydrostatic stress superposed onto a given deviatoric loading affects the strain to failure. This hypothesis has been verified experimentally. However, to go further and understand the driving mechanisms behind this finding, access into the complex stress and strain distributions that an amorphous polymer experiences during multi-axial loading conditions was necessary. As a result, recourse to numerical simulation tools was evident. However, these simulations, and the knowledge gained from them, are limited by the accuracy of the constitutive model used to define the behavior of the material. Indeed, polymeric materials exhibit some very peculiar deformation behavior. The material intrinsic behavior is not only strongly dependent upon temperature, strain rate and hydrostatic pressure (appendix A, fig. 38, 39 and 40) but also exhibit small-strain softening as well as large-strain hardening. When using such tools, it is therefore paramount to incorporate all those behaviors, specific to amorphous polymers, into the material model. Resulting from approximately 40 years of collaborative work on modeling complex glassy polymer behavior, the so-called macromolecular model, presented in chapter III, was the ideal candidate. Over the years, this sophisticated physics-based model has evolved thanks to many renowned researchers and is now able to depict realistically the complex deformation behavior of amorphous polymers. Results from the calibrated macromolecular model showed very good agreements with the experimental notched bars responses at various levels of stress triaxiality, temperature and strain rate.

The primary purpose behind using notched bars in these experiments was to minimize the variations of the stress triaxiality ratio with respect to the deformation, so its effect on the fracture behavior can be quantified in a controllable manner. This has been done extensively for fracture studies on power law hardening materials such

as metals. The experimental work introduced in this thesis, and more particularly the design and geometry of the notched specimens, was based on previous studies of ductile fracture for metals. The expectations were to achieve minor triaxiality variations as well as a large enough range so the fracture mechanisms affected by the levels of stress triaxiality would be easier to differentiate. However, The intrinsic deformation behavior of polymers does not obey power laws and the findings presented in chapter IV have proven that this particular specimen design was not well suited for the purpose mentioned above. When a more complex material model, one that is able to realistically describe polymeric deformation behavior, was used for the numerical simulations, it appeared that the stress triaxiality distribution across the specimen mid-section and throughout deformation was clearly not "minimized" as initially expected. Moreover, it has been shown that a minor change in the specimen geometry, which occurred during the manufacturing stage, caused significant reductions in the range of stress triaxiality achieved by these modified samples.

A fracture model was presented in chapter V. The model is based on experimental works and is essentially empirical in nature. The initiation fracture criterion has the main advantage of being simple to implement with a straightforward procedure to identify the two temperature dependent material parameters. It is also able to account for pressure sensitivity. Results have shown that in terms of accuracy, the criterion yields predictions that tend to worsen as the strain rate changes further away from the calibrated conditions. Part of this could be assigned to the scatter observed in the experimental data across the range of notch acuities, temperatures and strain rates considered. As mentioned above, the rationale for the notched bar tensile tests was to vary, in a controlled manner, the stress triaxiality and thus being able to calibrate the pressure sensitive fracture criterion. Therefore, another source of inaccuracy in the predictions could also be due to the strong variations in the

triaxiality as well as the smaller range achieved.

The effects of physical aging on the fracture behavior have also been investigated. It was observed that while the effect of aging on tensile strength is moderate, its effect seems to be more pronounced for conditions favoring more ductile conditions, such as a lower level of stress triaxiality. Also, the strain to failure was significantly affected by aging. Aged specimens consistently exhibited a lower strain to failure compared to there unaged counterparts, regardless of the conditions of temperature, strain rate and notch acuity. In addition, the fracture locus corresponding to the aged specimens seemed to be flattened. The extent of the influence of aging on the fracture behavior seems to be strongly correlated with the temperature. A higher testing temperature increases the influence of aging on the strain to failure which occurs in a more brittle manner.

Ultimately, the goal would be to design a specimen where ideally the distribution across the specimen mid-section and throughout deformation of the stress triaxiality would be constant so the fracture mechanisms affected by the levels of stress triaxiality would be easier to differentiate. Also, this would allow the calibration of the fracture model presented in this thesis, including the damage evolution model. Finally, the implementation of aging effects into the physics-based macromolecular deformation model as well as in the heuristic fracture model presented earlier, through appropriate internal state variables, would allow the design and development of more durable polymers and polymer-based composite materials through out their life-cycle.

REFERENCES

[1] X. Poulain, Modeling inelasticity and fracture of polymers with applications to composites, Ph.D. dissertation, Texas A&M University, College Station TX (2010).

[2] T. Wang, K. Kishimoto, M. Notomi, A micromechanics criterion for the ductile fracture of a polycarbonate, Key Eng. Mat. 183-1 (2000) 121–126.

[3] E. Kong, Physical aging in epoxy matrices and composites, Advances in Polymer Science 80 (1980) 125–171.

[4] M. Sambasivam, A. Klein, L. Sperling, Energy-consuming micromechanisms in the fracture of glassy-polymers .2. effect of molecular-weight on the fracture of polystyrene, Macromolecules 28 (1995) 152–159.

[5] P. Bowden, S. Raha, Formation of micro-shear bands in polystyrene and polymethylmethacrylate, Phil. Mag. 22 (1970) 463.

[6] T. Brady, G. Yeh, Yielding behavior of glassy amorphous polymers, J. App. Phys. 42 (1971) 4622.

[7] A. Argon, J. Hannoosh, Initiation of crazes in polystyrene, Phil. Mag. 36 (1977) 1195–1216.

[8] E. Kramer, A. Donald, The mechanism for craze-tip advance in glassy-polymers, Phil. Mag. 43 (1981) 857–870.

[9] J. Trent, I. Palley, E. Baer, Relationships between mechanical-behavior and craze morphology in thin-films of polystyrene, J. Mat. Sci. 16 (1981) 331–340.

[10] L. Asp, L. Berglund, R. Talreja, A criterion for crack initiation in glassy polymers subjected to a composite-like stress state, Comp. Sci. Tech. 56 (11) (1996) 1291–1301.

[11] A. Mackenzie, J. Hancock, D. Brown, On the influence of state of stress on ductile failure initiation in high strength steels, Eng. Frac. Mech. 9 (1) (1977) 167–188.

[12] G. R. Johnson, W. H. Cook, Fracture characteristics of three metals subjected to various strains, strain rates, temperatures and pressures, Eng. Frac. Mech. 21 (1) (1985) 31–48.

[13] Y. Bao, T. Wierzbicki, On fracture locus in the equivalent strain and stress triaxiality space, Int. J. Mech. Sci. 46 (2004) 81–98.

[14] A. Benzerga, J. Besson, A. Pineau, Anisotropic ductile fracture part 1: experiments, Acta Mater. 52 (2004) 4623–4638.

[15] P. Bridgman, Studies in Large Plastic Flow and Fracture, McGraw-Hill, New York, 1952.

[16] M. Sobieraj, S. Kurtz, C. Rimnac, Notch strengthening and hardening behavior of conventional and highly crosslinked uhmwpe under applied tensile loading, Biomaterials 26 (2005) 3411–3426.

[17] R. Kody, A. Lesser, Deformation and yield of epoxy networks in constrained states of stress, J. Mat. Sci. 32 (1997) 5637–5643.

[18] Y. Hu, Z. Xia, F. Ellyin, The failure behavior of an epoxy resin subject to multiaxial loading, Proceedings of the Pipeline Division Specialty Conference 211 (2006) 1–8.

[19] L. C. E. Struik, Physical aging in amorphous polymers and other materials, Elsevier, Amsterdam, 1978.

[20] C. G"Sell, G. B. McKenna, Influence of physical ageing on the yield response of dgeba/poly(propylene) oxide epoxy glasses, Polymer 33 (1992) 2103–2113.

[21] G. B. McKenna, J. M. Crissman, A. Lee, Relationships between failure and other time dependent processes in polymeric materials, American Chemical Society, Polymer Preprints, Division of Polymer Chemistry 29 (1988) 128–129.

[22] S. Belbachir, F. Zairi, G. Ayoub, U. Maschke, M. Nait-Abdelaziz, J. M. Gloaguen, M. Benguediab, J. Lefebvre, Modelling of photodegradation effect on elastic-viscoplastic behavior of amorphous polyactic acid films, J. Mech. Phys. Solids 58 (2) (2010) 241–255.

[23] J. Williams, Fracture mechanics of polymers, Poly. Eng. Sci. 17 (1077) 144–149.

[24] A. Kinloch, Mechanics and mechanisms of fracture of thermosetting epoxy polymers, Advances in Polymer Science 72 (1985) 45–67.

[25] R. Estevez, M. Tijssens, E. Van der Giessen, Modeling of the competition between shear yielding and crazing in glassy polymers, J. Mech. Phys. Solids 48.

[26] S. Sternstein, L. Ongchin, Yield criteria for plastic deformation of glassy high polymers in general stress fields, Polymer Preprints 10 (1969) 1117–1124.

[27] S. Sternstein, F. Meyers, Yielding of glassy polymers in the second quadrant of principal stress space, J. Macro. Sci. B8 (1973) 539–571.

[28] R. Oxborough, P. Bowden, A general critical-strain criterion for crazing in amorphous polymers, Phil. Mag. 28 (1973) 547–559.

[29] B. Gearing, L. Anand, On modeling the deformation and fracture response of glassy polymers due to shear-yielding and crazing, Int. J. Solids Structures 41 (2004) 3125–3150.

[30] K. Chowdhury, Damage initiation, progression and failure of polymer matrix composites due to manufacturing induced defects, Ph.D. dissertation, Texas A&M University, College Station, Texas (2007).

[31] K. Chowdhury, R. Talreja, A. Benzerga, Effects of manufacturing-induced voids on local failure in polymer-based composites, J. Eng. Mat. Tech. 130 (021010).

[32] A. Benzerga, J.-B. Leblond, Ductile fracture by void growth to coalescence, Advances in Applied Mechanics 44 (2010) 169–305.

[33] J. D. Littell, C. R. Ruggeri, R. G. Goldberg, G. R. Roberts, W. A. Arnold, W. K. Binienda, Measurement of epoxy resin tension, compression, and shear stress-strain curves over a wide range of strain rates using small test specimens, Journal of Aerospace Engineering 21 (2008) 162–173.

[34] R. Haward, G. Thackray, The use of a mathematical model to describe isothermal stress-strain curves in glassy thermoplastics, Proc. Roy. Soc. London A 302 (1968) 453–472.

[35] A. Argon, A theory for the low temperature plastic deformation of glassy polymers, Phil. Mag. 15 (1973) 28–39.

[36] M. Boyce, D. Parks, A. Argon, Large inelastic deformation of glassy polymers. part i: Rate dependent constitutive model, Mechanics of Materials 7 (1988) 15–33.

[37] E. Arruda, M. Boyce, R. Jayachandran, Effects of strain rate, temperature and thermomechanical coupling on the finite strain deformation of glassy polymers, Mechanics of Materials 19 (1995) 193–212.

[38] P. D. Wu, E. Van der Giessen, On improved network models for rubber elasticity and their applications to orientation hardening in glassy polymers, J. Mech. Phys. Solids 41 (1993) 427–456.

[39] P. D. Wu, E. Van der Giessen, Computational aspects of localized deformations in amorphous glassy polymers, Eur. J. Mech. 15 (1996) 799–823.

[40] E. Arruda, M. Boyce, A three-dimensional constitutive model for large stretch behaviour of rubber materials, J. Mech. Phys. Solids 41 (1993) 389–412.

[41] S. Kweon, A. Benzerga, To be submitted, Int. J. Plasticity.

[42] E. Klompen, T. Engels, L. Govaert, H. Meijer, Modeling of the postyield response of glassy polymers: Influence of thermomechanical history, Macromolecules 38 (2005) 6997–7008.

APPENDIX A

ADDITIONAL EXPERIMENTAL RESULTS - UNAGED SPECIMENS

(a)

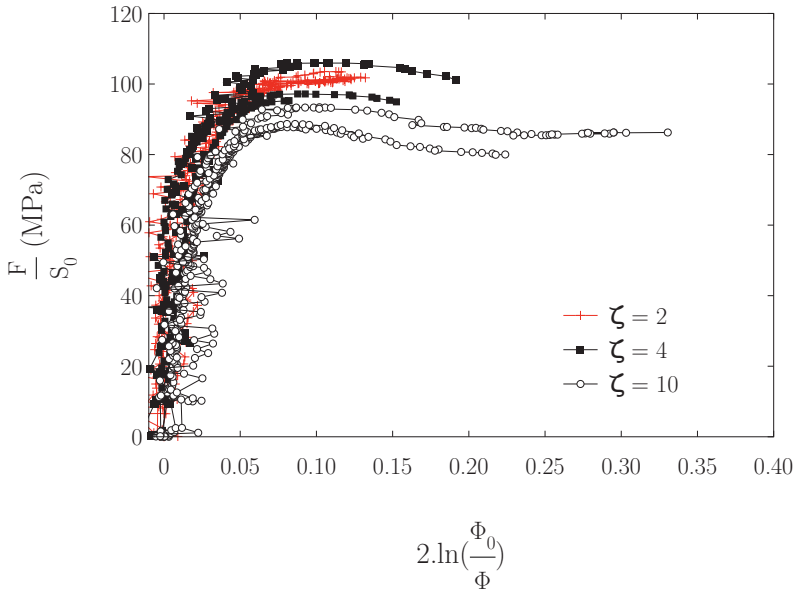

(b)

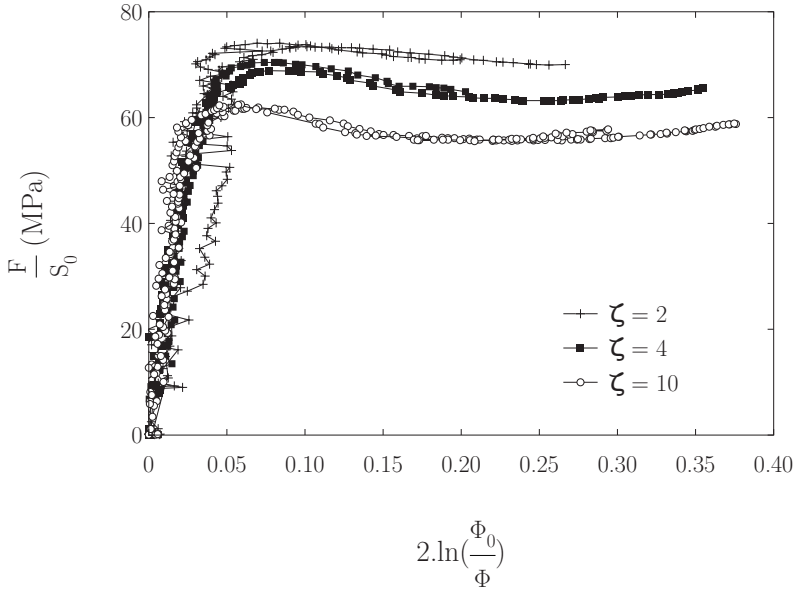

Fig. 36. Normalized load versus minimal cross-section mean strain at $\dot{\epsilon} = 10^{-3}$/s for various levels of triaxiality, (a) $T = 25°$C. (b) $T = 80°$C.

(a)

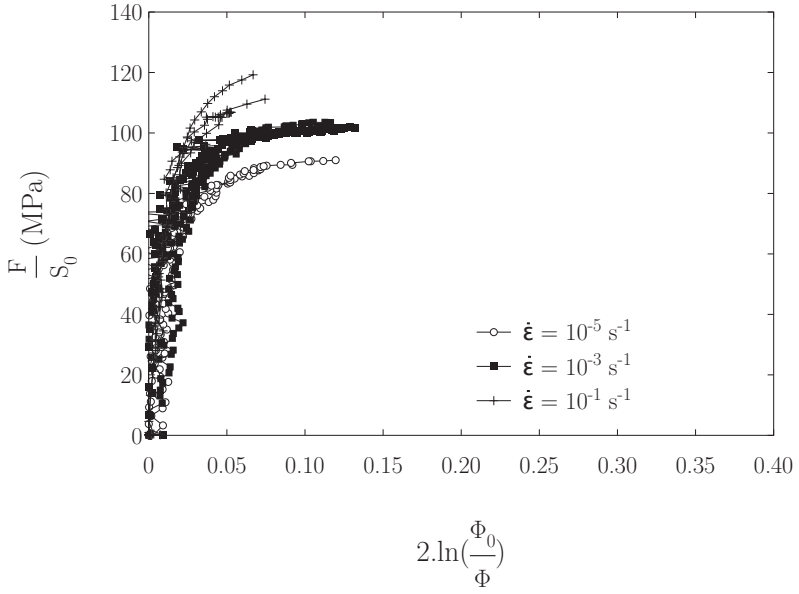

(b)

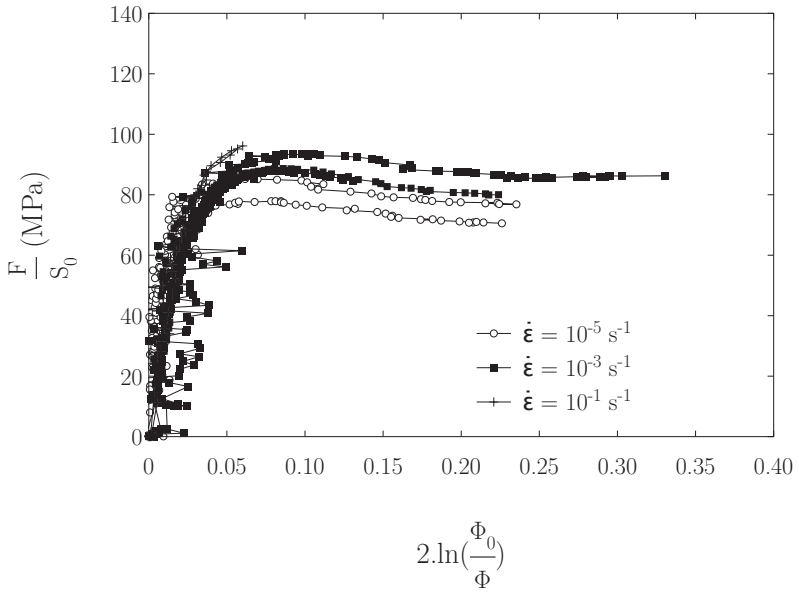

Fig. 37. Normalized load versus minimal cross-section mean strain at $T = 25°\text{C}$ for various levels of strain rate, (a) $\zeta = 2$. (b) $\zeta = 10$.

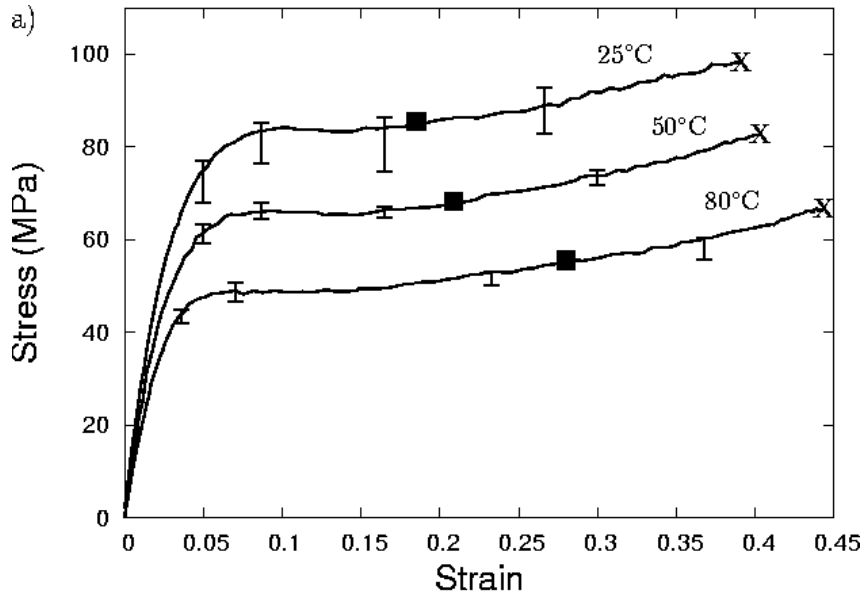

Fig. 38. Temperature effects under tension for smooth bar at $\dot{\epsilon} = 10^{-3}/\text{s}$ [1].

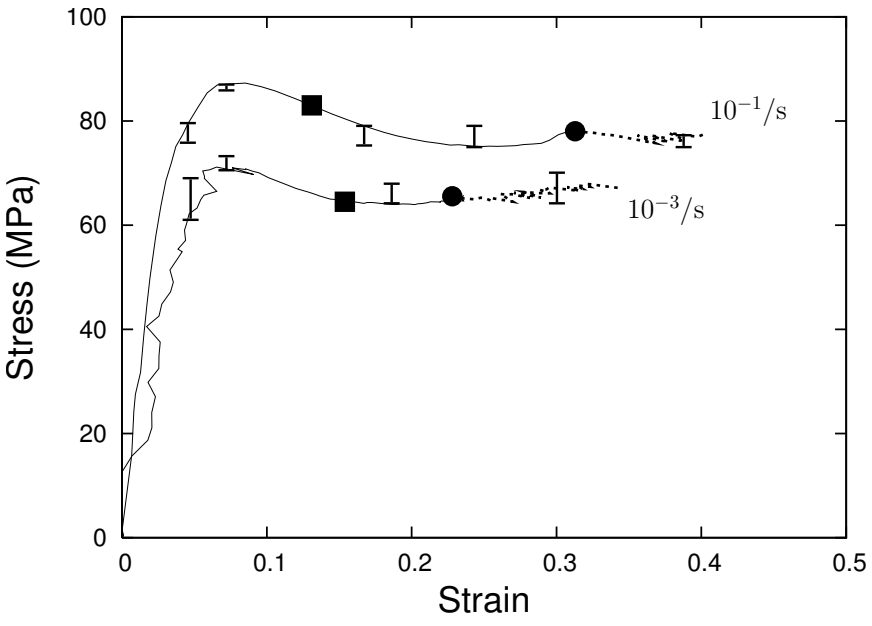

Fig. 39. Strain-rate effects under compression for smooth bar at $T = 50°\text{C}$ [1].

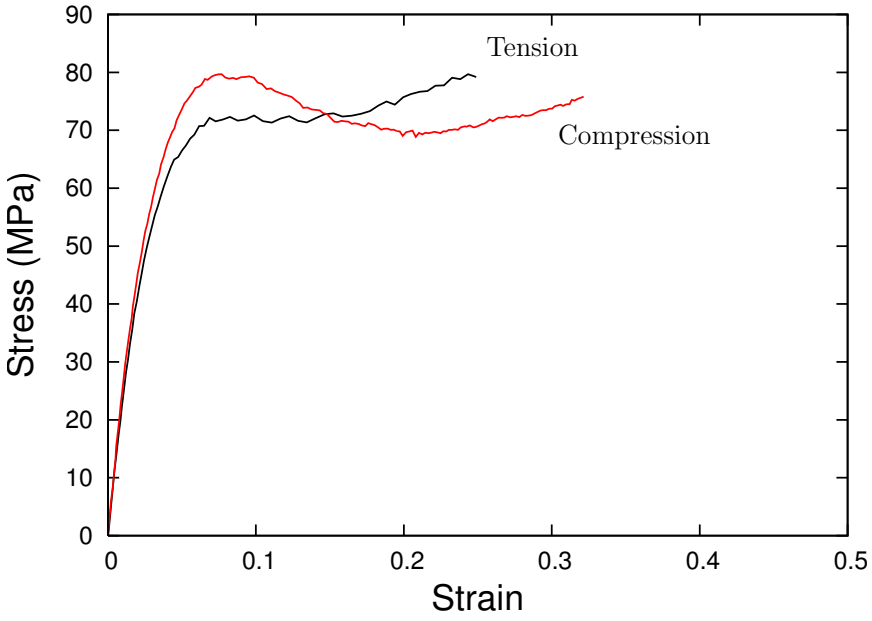

Fig. 40. Stress-strain curves under compression and tension for smooth bars at $T = 25°\text{C}$ and $\dot{\epsilon} = 10^{-5}/\text{s}$ [1].

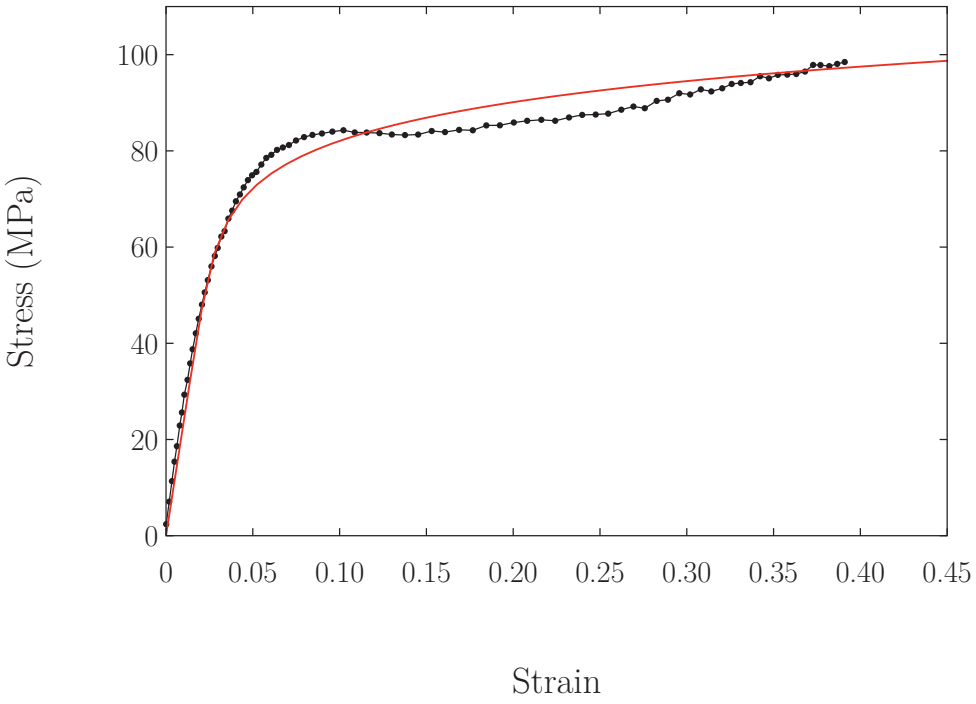

Fig. 41. Stress-strain curves under tension for smooth bars at $T = 25°\text{C}$ and $\dot{\epsilon} = 10^{-3}/\text{s}$. Black dotted curve and red curve represent the experimental response and finite element result for a power law hardening material.

APPENDIX B

ADDITIONAL EXPERIMENTAL RESULTS - AGED SPECIMENS

(a)

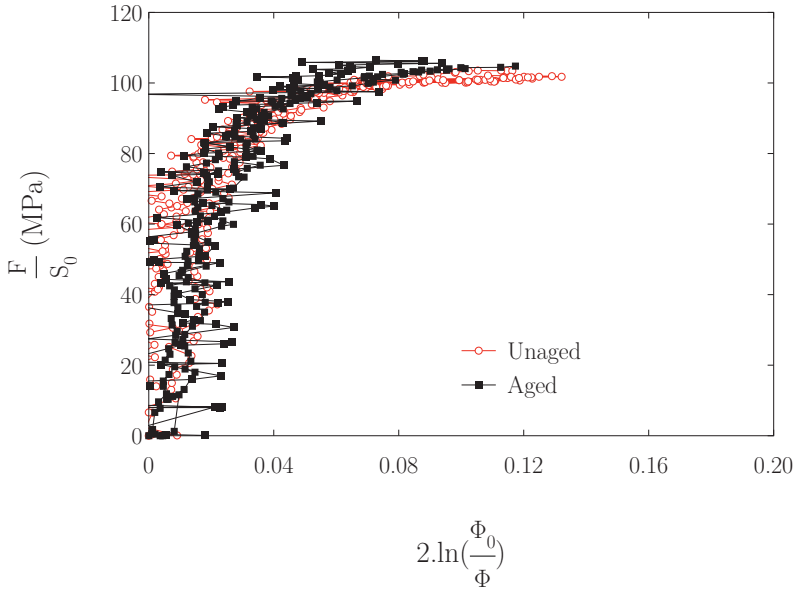

(b)

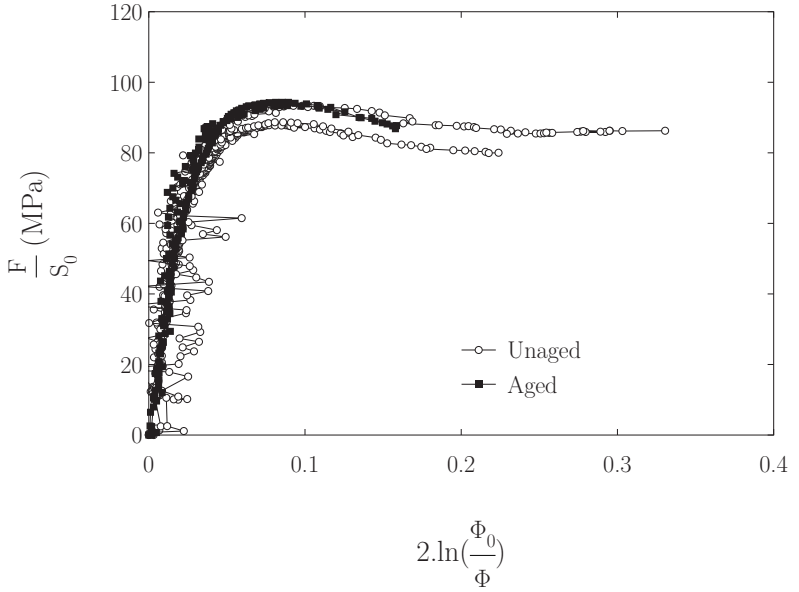

Fig. 42. Normalized load versus minimal cross-section mean strain for aged specimens captured at $T = 25°\text{C}$ and $\dot{\epsilon} = 10^{-3}/\text{s}$ for various levels of triaxiality, (a) $\zeta = 2$ (b) $\zeta = 10$.

VITA

Name:

Anthony De Castro

Address:

Texas A&M University

Department of Aerospace Engineering

H.R. Bright Building

3141 TAMU College Station, TX 77843-3141

Email Address:

adecastr@neo.tamu.edu

Education:

B.S., Mechanical Engineering, Université de Technologie de Compiègne, France, 2006

M.S., Aerospace Engineering, Texas A&M University, USA, 2010

Experience:

Commissioning & Start-up Engineer, Technip, USA, 2007

Risk Management Coordinator, Saipem, Kazakhstan, 2006

CAD Designer, Diethelm Keller Aviation, Singapore, 2005

The typist for this thesis was Anthony De Castro.